Федеральное государственное автономное образовательное учреждение
высшего образования «Уральский федеральный университет
имени первого Президента России Б.Н. Ельцина»
Физико-технологический институт
Кафедра экспериментальной физики

На правах рукописи

Хоссени Уиссам Адел Лотфи

АДИАБАТИЧЕСКИЙ ПОТЕНЦИАЛ ЯН-ТЕЛЛЕРОВСКИХ КОМПЛЕКСОВ В КРИСТАЛЛАХ СО СТРУКТУРОЙ ФЛЮОРИТА

1.3.8. Физика конденсированного состояния

Диссертация на соискание ученой степени
кандидата физико-математических наук

Научный руководитель:
доктор физико-математических наук,
профессор
Гудков Владимир Васильевич

Екатеринбург 2023

Federal State Autonomous Educational Institution of Higher Education «Ural Federal University
named after the first President of Russia B.N. Yeltsin»
Institute of Physics and Technology
Department of physical methods and quality control devices
Department of experimental physics

As a manuscript

Hosseny Wessam Adel Lotfy

ADIABATIC POTENTIAL ENERGY SURFACE OF THE JAHN-TELLER COMPLEXES IN FLUORITE-STRUCTURE CRYSTALS

1.3.8. Condensed matter physics

Dissertation for the degree of candidate of
physical and mathematical sciences

Supervisor
Doctor of physical and mathematical sciences,
Professor
Gudkov Vladimir Vasilyevich

Yekaterinburg –2023

TABLE OF CONTENTS

LIST OF MOST IMPORTANT SYMBOLS

α_β attenuation coefficient of β mode

β indication of the normal mode or of the component of elastic moduli tensor

ε_{ij} , ε_k deformation tensor component

ρ density of the crystals

σ_{ij} elastic stress tensor component

τ relaxation time

ω circular frequency of a wave

ω_R radial vibronic frequency

ω_τ trigonal vibrational frequency

a_0 distance between the JT ion and the nearest neighbor (fluorine ion)

c_{44} trigonal elastic modulus

c_β c_{ij} , c_{ijkl} component of the elastic moduli tensor

c_E tetragonal elastic modulus

E^E tetragonal JT stabilization energy

E^{OR} orthorhombic JT stabilization energy

E^T trigonal JT stabilization energy

F_E tetragonal linear vibronic coupling constant

F_T trigonal linear vibronic coupling constant

k_B Boltzmann constant

k_β wave number of the β mode

K_β primary force constant

M reduced mass of JT complex

n concentration of 3d ions

Q_n^{OR} positions of the six orthorhombic minimum (n = 1,….6)

Q_ϑ, Q_ε tetragonal symmetrized coordinates

Q_ξ, Q_ζ, Q_η trigonal symmetrized coordinates

u_i displacement vector component

v_β phase velocity of the β normal mode

V_0 activation energy

W_{ET} quadratic vibronic coupling constant

LIST OF ABBREVIATION

APES – adiabatic potential energy surface

ESR – electron spin resonance

JT – Jahn-Teller

JTE – Jahn-Teller effect

INTRODUCTION

Relevance of the topic. The Jahn–Teller effect (JTE) [1] plays an important role in shaping the structure of molecules and crystals and influencing their physical properties. It is discussed in the study of magnetic materials [2-6], perovskites [7-11], multiferroics [12-15], graphenes [16], fullerenes [17], and laser crystals [18-21]. In crystals, the JTE exists in two variants: as a cooperative effect, where Jahn -Teller (JT) centers are implemented in the crystal lattice, or as a phenomenon in a system of non-interacting complexes initiated by vacancies or impurities, often represented by 3*d* ions as cationic substitution. Such crystals and especially fluorites, those gave the name to the phenomenon known as fluorescence [22], attract outstanding interest and are used in optical devices [23-25] . Transition metal ions with an orbital degenerate state manifest the JTE and, therefore, have a much more complicated electronic structure [26]. Quantitative information about the electron-lattice interaction and the electronic structure [27] is mandatory for the use of these crystals in electronic and optical devices. Thus, the study of adiabatic potential energy surface (APES) of the JT complexes is an urgent task, both in terms of fundamental research and with respect to practical applications.

The degree of development of the research topic. Traditional methods for investigation of the JTE in the impurity crystals are the study of optical emission and absorption spectra, electron spin resonance (ESR) and spin echo methods [28-31]. Physical acoustics experiments, commonly used in physics of solid state (see, e.g., [32]), cannot be considered as traditional methods of JTE research, albeit the first publications in this field date back to the 1960s (see review by Sturge [33], paragraph 9). At first, the experiments were performed using a resonance method: mechanical resonance of a specimen of Al_2O_3 doped with Ni^{3+} ions at about 2 MHz [34]. More accurate attenuation measurements were performed at a higher frequency using the echo pulse method [35]. Nevertheless, in an ultrasonic experiment, the excitation frequency is still too low to arrange the resonant transitions between the energy levels of the JTT complex. Consequently, the

ultrasonic energy dissipation and dispersion conditioned by the JTE are of a relaxation nature and relate only to the lowest energy (ground) state.

Relaxation emerges as a result of the non-equilibrium distribution initiated by an ultrasonic wave in the system of the JT complexes which represent a thermodynamic ensemble. Within the framework of the phenomenological approach, the process of relaxation is characterized by the relaxation time. It can be obtained in an ultrasound experiment if an external parameter (temperature, magnetic field, etc.) significantly changes its value. The relaxation time temperature dependence gives information about the relaxation mechanisms conditioned by the properties of JT complexes. This dependence was a valuable achievement of the JTE study by the primary ultrasound experiments. It cannot be obtained by ESR and optical methods: in ESR, the spin-spin and spin-lattice relaxation are studied, while in optical spectra, transitions between the ground and excited states are investigated.

Recent ultrasound studies of the impurity compounds have shown new advantages for providing quantitative data on the parameters of the JT complexes (see [36, 37] and references therein). If the symmetry of the deformations created by the wave corresponds to the symmetry of the local vibrational mode, a new channel of energy dissipation arises. The study conducted with waves of various polarizations gives an exceptional opportunity to reveal the active local modes and, consequently, the symmetry properties of global minima of the lowest sheet of the APES.

Purpose and objectives of the work. The purpose of the thesis is a comprehensive study of the symmetry properties of the global minima and saddle points of the JT complexes in crystals with a fluorite structure doped with 3*d* ions; basing on experimental data, to calculate the JT stabilization energies and the coordinates of the APES extrema defined in a 5-dimensional coordinate system corresponding to the symmetrized (trigonal and tetragonal) deformations of the cubic JT complex.

To achieve the goal of the work, the following tasks were solved:

1. Calculation of the linear and quadratic constants of the vibronic coupling, the stabilization energies and the coordinates of the APES extrema of the JT complex in the $SrF_2:Cr^{2+}$ crystal.

2. Analysis of the results of studies of the temperature dependences of attenuation of normal modes in the $CaF_2:Cr^{2+}$ crystal. Determination of the symmetry properties of the APES global minima and saddle points. Calculation of the vibronic coupling constants, the JT stabilization energies and coordinates of the APES extrema.

3. Analysis of the results of studies of the temperature dependences of attenuation of normal modes in the $CaF_2:Ni^{2+}$ crystal. Determination of the symmetry properties of the APES global minima and saddle points. Calculation of the vibronic coupling constants, the JT stabilization energies and coordinates of the APES extrema.

4. Analysis of the results of studies of the temperature dependences of attenuation of normal modes in the $CaF_2:Cu^{2+}$ crystal. Determination of the symmetry properties of the APES global minima and saddle points. Calculation of the vibronic coupling constants, the JT stabilization energies and coordinates of the APES extrema.

5. Revealing common properties and differences of the JT complexes in the studied compounds.

Scientific novelty:

1. It was found that the APES of the JT complexes of all crystals studied by us which possess a fluorite structure with isovalent substitution of a cation by a transition metal ion, namely, $SrF_2:Cr^{2+}$, $CaF_2:Cr^2$ [free ion configuration d^4, orbital term of the JT ion ${}^5T_{2g}\left(e_g^2t_{2g}^2\right)$], $CaF_2:Cu^{2+}$ [d^9, ${}^2T_{2g}\left(e_g^4t_{2g}^5\right)$] and $CaF_2:Ni^{2+}$ [d^8, ${}^3T_{1g}\left(e_g^4t_{2g}^4\right)$] is described by the quadratic $T\otimes(e+t_2)$ JTE problem, i.e., has the APES global minima of orthorhombic symmetry. The smallest potential barriers are formed by the trigonal saddle points, and the largest are formed by the tetragonal ones.

2. Quantitative data on the linear and quadratic vibronic coupling constants, JT stabilization energies, coordinates of the APES extrema in a 5-dimensional system of symmetrized displacements were obtained.

3. On the basis of ultrasound data, the APES parameters were calculated and ones independent of the concentration of JT ions are found: the activation energy V_0 and the ratio of the linear vibronic coupling constants $|F_T / F_E|$ by which the studied crystals were compared.

Theoretical and practical significance of the work:

1. The method used for determination of the symmetry properties of the APES has shown its efficiency and unambiguity of the results. It can be recommended for usage in further investigation of the APES in doped crystals by means of ultrasonic experiment.

2. The obtained results expand the fundamental understanding of the mechanism of the APES construction in the case of triply degenerate orbital states: four nearest neighbors lead to tetragonal APES global minima, eight lead to orthorhombic ones.

3. The ratio of the linear vibronic coupling constants $|F_T / F_E|$ is close to unit and the assumption of $|F_T| \approx |F_E|$ can be appropriately used in model calculation of the APES in the case when only one vibronic coupling constant is defined in an experiment.

Methodology and research methods. The methodology of the APES parameters evaluation in a cubic crystal is based on the physical acoustics research method. It implies the use of the data on temperature dependences of attenuation and phase velocity of the normal modes: the two transverse waves (or one transverse and one longitudinal modes) propagating along the [110] crystallographic axes. Anomalies in all the studied modes indicate the orthorhombic symmetry of the APES global minima, ones in tetragonal reveals the tetragonal symmetry of the APES global minima, while the anomalies in trigonal mode justify the trigonal symmetry of the APES global minima.

After extraction of the JT contribution to ultrasonic attenuation, the temperature dependence of relaxation time is constructed and the linear vibronic coupling constants are evaluated. Simulation of the temperature dependence of the relaxation time with three mechanisms (thermal activation, tunneling through the potential energy barrier, and two-phonon mechanisms [33]) reveals the magnitude of the activation energy which makes it possible to calculate the value of the potential energy barrier which is the lowest saddle point. The evaluated magnitudes of the linear vibronic coupling constants allows to calculate the magnitudes of the corresponding JT stabilization energies. The coordinates of the APES global minima are calculated with the use of expressions given in section 3.3 in [38] or in the case of the orthorhombic global minima the expressions published in [39].

Thesis to defend:

1. The APES of the JT complexes in crystals with a fluorite structure with isovalent substitution of a cation by a transition metal ion, $CaF_2:Cr^{2+}$, $CaF_2:Cu^{2+}$, and $CaF_2:Ni^{2+}$ is described by the quadratic JTE problem, i.e., it has the orthorhombic global minima, the smallest potential barriers are formed by the trigonal saddle points, and the largest ones have the tetragonal symmetry.

2. The parameters of the APES calculated on the basis of ultrasonic data and independent of the concentration of the JT ions are the activation energy and the ratio of linear constants of vibronic coupling. In most compounds, the activation energy varies in the range of 90 – 400 cm^{-1}.

3. The isothermal JT contribution to all the elastic moduli in a cubic crystal depends on both tetragonal and trigonal linear vibronic coupling constants if the complex undergoes static deformation along at least one of the cubic axes.

The degree of reliability of the work results is determined by the use of the data obtained on the certified experimental setups and certified computer programs. The results obtained during the work which can be compared with the optical experiments or ESR are in good agreement with the published literature data.

Approbation of work

The main results of the dissertation were presented and discussed at 6 Russian or international conferences, congresses, symposia.

They are XIV Russian Conference in Semiconductor Physics. (Novisibirsk, Russian Federation, RCS – 2019), XXIII Ural International Winter School on Semiconductor Physics. (Yekaterinburg, Russian Federation, UIWSPS- 2020), VII International Youth Scientific Conference Physics. Technology. Innovations. (Yekaterinburg, Russian Federation, 2020), Scientific Session NRNU MEFI on the Direction Innovative Nuclear Technologies. (Snezhinsk, Russian Federation, NRNU MEFI -2020), VIII International Youth Scientific Conference Physics. Technology. Innovations. (Yekaterinburg, Russian Federation, PTI-2021), IX International Youth Scientific Conference Physics. Technology. Innovations. 16-20 May, 2022, Yekaterinburg, Russian Federation, PTI-2022.

Personal contribution of the author. The subject of the dissertation and the research objects was suggested by the supervisor. Experiments on ultrasonic attenuation were carried out by M.N. Sarychev with the help of the author of the thesis.

The author has carried out the whole complex of calculations, including composition of the program for the data processing which was used for evaluation of the parameters of the APES of the studied JT complexes. The author took a decisive part in the preparation of scientific publications and in person presented 6 reports at the conferences listed above.

The studied crystals were grown at E.K. Zavoisky Physical-Technical Institute, Kazan Scientific Center of the RAS by prof. V.A. Ulanov and at A.P. Vinogradov Institute of Geochemistry, Siberian Branch of the RAS by prof. A.V. Egranov. Composition of the specimens was examined by V.T. Surikov.

Publications. On the theme of the dissertation, the author has published 3 articles indexed in the international databases Scopus and WoS, included in the list of the Higher Attestation Commission, and 2 papers in AIP Conference Proceeding indexed in Scopus.

The structure and scope of the dissertation. The dissertation contains an introduction, 5 chapters, a conclusion and a list of references. The volume of the dissertation is 85 pages, including 22 figures, 13 tables and a bibliographic list of 83 items and list of main publications on the dissertation topic (papers – 5 items and conference reports - 6 items).

CHAPTER 1. LITERATURE REVIEW

1.1. Historical overview

Currently, the term JTE is used for a whole range of phenomena, one way or another, related to the theorem formulated by Hermann Arthur Jahn and Edward Teller in 1937 [1]. In literature (see, for example, [38]), the case is mentioned of Teller discussion of the results of the experiment done by his graduate student Rudolf Renner [40] with Lev Landau in 1934. Renner's research served as an impetus for considering molecules with degenerate orbital states. A qualitative picture of the phenomenon was constructed, for the mathematical description of which Teller turned to Jahn, which eventually led to the aforementioned theorem, which is called the Jahn-Teller theorem.

The theorem states that the highly symmetric state of a molecule with the orbital degeneracy is unstable, and a stable state is achieved due to deformations that lower the symmetry of the molecule. Subsequently, it became clear that this theorem also applies to crystals in which the JT centers are contained in an elementary cell, as well as to crystals doped with the JT ions. For a long time, the JTE was the subject of theoretical research [41 – 43], and it was even believed that it was not experimentally observable [44]. However, in the 1950s, experimental works appeared on the study of ESR spectra [45- 47] and optical absorption spectra [48], in which the interpretation of the results was impossible without involving ideas about JTE (see reviews [33], [49] and bibliographic review [50]).

1.2. Basics of the JTE theory

The theoretical description of the JTE is based on the solution of the Schrodinger equation with the Hamiltonian

$$H = H_r + H_Q + V(r,Q) \ , \tag{1.1}$$

where H_r represents the kinetic energy of electrons and the inter-electronic interaction, H_Q is the kinetic energy of nuclei, r and Q are the sets of electronic and nuclear coordinates, respectively. The operator of the interaction of electrons

and nuclei $V(r,Q)$ is written as power series over displacements of the nuclei relative to the initial configuration with $Q_\alpha = Q_{\alpha 0} = 0$. The total wave function $\Psi(r,Q)$ is written as series over electronic wave functions $\varphi_k(r)$:

$$\Psi(r,Q) = \sum_k \chi_k(Q) \cdot \varphi_k(r) \,, \tag{1.2}$$

A system of coupled equations with coefficients $\chi_k(Q)$

$$\left[H_Q - E_k(Q) - E\right]\chi_k(Q) + \sum_{m \neq k} W_{km}(Q)\chi_m(Q), \tag{1.3}$$

is a solution of the Schrodinger equation in which the vibronic coupling operator

$$W(Q) = V(r,Q) - V(r,0) = \sum_\alpha \left(\frac{\partial V}{\partial Q_\alpha}\right)_0 Q_\alpha + \frac{1}{2}\sum_{\alpha,\beta}\left(\frac{\partial^2 V}{\partial Q_\alpha \partial Q_\beta}\right)_0 Q_\alpha Q_\beta + \ldots \,. \tag{1.4}$$

The matrix elements of the operator W are entering the expression for the adiabatic potential (the potential energy of the nuclei of the JT complex in the averaged field of electrons in the state described by $\varphi_k(r)$)

$$E_k(Q) = E_k'(Q) + W_{kk}(Q), \tag{1.5}$$

where $E_k'(Q)$ is the energy of elastic deformations of the complex without taking into account the vibronic coupling.

In the case of a two-fold orbital degeneracy, the APES is given in the system of tetragonal symmetrized coordinates Q_ϑ and Q_ε in the Ham notation [51] and its minima (stabilization energy)

$$E_E^{JT} = \frac{F_E^2}{2K_E}. \tag{1.6}$$

They are determined by the tetragonal linear constant of the vibronic coupling F_E and the primary tetragonal force constant K_E, which characterizes the elastic energy of the JT complex without taking into account the vibronic interaction.

$$F_E = \langle \vartheta | \left(\frac{\partial V}{\partial Q_\vartheta}\right) | \vartheta \rangle \,. \tag{1.7}$$

In the case of three-fold orbital degeneracy, in the general case, the APES is given in a 5-dimensional system of symmetrized coordinates, tetragonal (mentioned above) and trigonal Q_ξ , Q_ζ and Q_η in Ham's notation [51]. The minima of trigonal symmetry (if any) are given by the trigonal linear constant of the vibronic coupling F_T and the primary trigonal force constant K_T:

$$E_T^{JT} = \frac{2}{3}\frac{F_T^2}{K_T} \ , \tag{1.8}$$

$$F_T = \langle \eta | \left(\frac{\partial V}{\partial Q_\eta} \right) | \eta \rangle . \tag{1.9}$$

The description of the JTE in doped crystals is based on a molecular model in which the JT complex containing the JT ion and the immediate environment is considered. At the same time, the concentration of JT ions should be small so that the complexes forming the thermodynamic ensemble (the JT subsystem of the crystal) can be considered as non-interacting with each other and described within the framework of the approach given above in this paragraph.

Within the framework of the phenomenological approach, the state of a subsystem can be described with the help of some thermodynamic potential. Bearing in mind that we will need to consider mechanical properties (absorption and dispersion of normal elastic modes, elastic modulus), it makes sense to use Helmholtz free energy $A = U - TS$, or rather, its density (see, for example, [52]). Further, by volume-dependent parameters, for example, internal energy U, entropy S, we will consider as the values of a unit volume, i.e., the density:

$$dA = \sigma_{ij} d\varepsilon_{ij} + E_i dD_i + H_i dB_i - SdT \ , \tag{1.10}$$

where σ_{ij} are the components of the elastic stress tensor, ε_{ij} are the components of the relative strain tensor, E_i are the electric field strength components, H_i are the magnetic field strength components, D_i are the electric induction components, B_i are the magnetic induction components and T is the temperature. It is obvious that the manifestation of JTE in the acoustic/ultrasonic experiment is described by the

first term in the right hand part [33], by the second in the optical studies [53], in the magnetic – by the third (magnetostatics [54], ESR [45], [47], [51]; [55]), and by the fourth in the thermal physics [54].

1.3. Physical acoustics method of investigation

In our work, we will limit ourselves to considering the first term in equation (1.10). However, equation (1.10) should be supplemented with material equations, which at zero electric and magnetic fields and at constant temperature are reduced to the following [56]:

$$\sigma_{ij} = c^{T}_{ijkl}\varepsilon_{kl}\,, \tag{1.11}$$

where

$$\varepsilon_{ij} = \frac{1}{2}\left(\frac{\partial u_i}{\partial x_j} + \frac{\partial u_j}{\partial x_i}\right), \tag{1.12}$$

u_i are the components of the displacement vector of the volume element, x_j are the components of the radius vector in the Cartesian coordinate system, and the components of the isothermal elastic moduli tensor are

$$c^{T}_{ijkl} = \left(\frac{\partial^2 A}{\partial\varepsilon_{ij}\partial\varepsilon_{kl}}\right)_{\varepsilon\to 0}. \tag{1.13}$$

The free energy density A is expressed using the partition function Z [57]:

$$A = -nk_B T\ln Z\,, \tag{1.14}$$

$$Z = \sum_k e^{-\frac{\Delta E_k}{k_B T}}\,, \tag{1.15}$$

where ΔE_k are variation of energy levels as a result of external effect of deformations, fields, temperature variations, k_B is the Boltzmann constant, n is concentration of structural elements.

Since the free energy of a crystal is an additive function, it also includes contribution of the JT subsystem. It is determined by equations (1.13) - (1.15) with parameters n, ΔE_k. As far as we know, Sturge and co-authors [35] were the first who, analyzing the results of ultrasound experiments on JTE, came to the conclusion about the relaxation nature of ultrasound attenuation due to the influence of the JT subsystem. Basing on the Zener equation [58] (see also [59]) they obtained an expression for the attenuation coefficient, which is given in the Sturge's review as follows (see page137 in [33]):

$$\alpha = \frac{1}{2} k_0 \frac{\left(c^{JT}\right)^S - \left(c^{JT}\right)^T}{c_0} \frac{\omega\tau}{1+\left(\omega\tau\right)^2} \ , \tag{1.16}$$

where k_0 and c_0 are some fixed values of the wave number and the corresponding dynamic modulus of elasticity (of the whole crystal), the superscripts S and T denote the adiabatic and isothermal contributions of the JT subsystem to the elastic modulus, ω is the cyclic frequency of the ultrasonic wave and τ is the relaxation time. This relaxation time characterizes the process of establishing the equilibrium state in a thermodynamic ensemble which is formed by the JT complexes (JT subsystem of a crystal). The state of the subsystem is described by the distribution function which takes into account different types of deformations of the JT complexes. So, relaxation means tendency to the equilibrium population of the states, corresponding to the distorted complexes. According to Sturge ([33], p.136), $\left(c^{JT}\right)^S$ is zero, while $\left(c^{JT}\right)^T$ is determined using the general expressions (1.13)-(1.15). In equation (1.16), the indices indicating the type of normal mode and the component of the tensor of elastic modules are omitted, which should correspond to the following definitions:

$$k = \frac{\omega}{v}, \tag{1.17}$$

$$c = \rho v^2, \tag{1.18}$$

where v is the phase velocity of the normal mode, ρ is the density of the crystal. Further description should be carried out by introducing a complex wave vector $\mathbf{k}$ and a tensor of complex dynamic moduli $\mathbf{c}$, whose changes caused by external parameters are determined as follows

$$\frac{\Delta k_\beta}{k_0} = -\frac{1}{2}\frac{\Delta c_\beta}{c_0}, \tag{1.19}$$

where the subscript β at k indicates the type of normal mode, and at c indicates the effective elastic modulus with which this mode is associated by the expression (1.18). The subscript 0, as before, denotes a fixed value of a physical quantity (for example, determined at the temperature $T = T_0$) and refers to the same mode or modulus β: $\Delta k_\beta = k_\beta - k_0$, $\Delta c_\beta = c_\beta - c_0$. If the variables vary with time and coordinates, as $\exp\left[i\left(\omega t - \mathbf{k}\cdot\mathbf{r}\right)\right]$, the complex wave vector is defined as

$$\mathbf{k} = \left(\frac{\omega}{v} - i\alpha\right)\mathbf{e}_\mathbf{k}, \tag{1.20}$$

where $\mathbf{e}_\mathbf{k}$ is the unit vector of $\mathbf{k}$ direction. Specifying the type of normal mode β will require specifying an subscript corresponding to this mode, for $\mathbf{k}$, v, and α. A more complete description of the manifestation of JTE in an ultrasound experiment (compared to equation (1.16)), including not only dissipation, but also dispersion, was given on page 748 in [60]:

$$\frac{k_\beta^{JT}}{k_0} = \left(-\frac{v_\beta^{JT}}{v_0} - i\frac{\alpha_\beta^{JT}}{k_0}\right) = -\frac{1}{2}\frac{c_\beta^{JT}}{c_0} = -\frac{1}{2}\frac{\left(c_\beta^{JT}\right)^T}{c_0}\frac{1 - i\omega\tau}{1 + \left(\omega\tau\right)^2}. \tag{1.21}$$

It follows from the above that the attenuation and phase velocity of normal elastic waves or the real and imaginary components of the tensor of dynamic elastic moduli associated with them are investigated by means of physical acoustics. Acoustic methods and schemes of experimental installations used for the study of solids are described in detail by McSkimin in [61]. From the variety given in this

chapter, we used a pulse method for measuring the phase velocity and attenuation of normal modes after passing through the investigated sample to study the JTE.

In installations operating on the principle of a frequency-variable bridge (see paragraph 3.1.2 in [62]), the change in phase velocity $\Delta v = v - v_0$ and the attenuation $\Delta\alpha = \alpha - \alpha_0$ coefficient are determined by the change in frequency $\Delta\omega = \omega - \omega_0$ necessary to maintain the balance of the bridge in phase and the change in the length of the sample caused by the external parameter $\Delta\ell = \ell - \ell_0$ and the voltage ratio at the receiver input U / U_0

$$\frac{\Delta v}{v_0} = -\mathrm{Re}\frac{\Delta k}{k_0} = \frac{\Delta\omega}{\omega_0} + \frac{\Delta\ell}{\ell_0}, \tag{1.22}$$

$$\Delta\alpha = -\frac{1}{\ell}\ln\frac{U}{U_0}. \tag{1.23}$$

In practice, the relative changes in the length of the sample from the external parameter are significantly less than the changes in other values, therefore, the last term in the right hand part in equation (1.22) is neglected, and the value ℓ_0 is used instead of ℓ in equation (1.23).

1.4. The degree of development of the research topic

As already noted in Introduction, the first experimental work on the study of JTE by ultrasonic technique dates back to the 60s of the 20th century and is associated with the name of Sturge (Michael Dudley Sturge 1931-2003) [53], [35]. Using an Al_2O_3: Ni^{3+} crystal as an example, he and his colleagues found that anomalies in the temperature dependences of attenuation have a relaxation nature, an expression for attenuation was obtained, from which it follows that there is a possibility to determine the temperature dependence of the relaxation time of the JT subsystem and calculating the values of the linear constants of the vibronic coupling. In addition, estimates were made of some values that determine the attenuation of

ultrasound due to the JT subsystem. That is, in principle, the direction of the JTE research has been set for a very distant future.

What was not done or not done accurately enough? In the expression for the relaxation time $\tau(T)$, the temperature T_1 corresponding to the condition $\omega\tau = 1$ was determined by the position T_m of the peak of relaxation attenuation. Since isothermal moduli are inversely proportional to temperature, it is an approximate value (valid at high temperatures). Besides, an expression for calculating the linear constant of the vibronic coupling was not obtained.

A direct continuation of the works by the Sturge group should be considered the studies of JTE by ultrasonic methods in compounds $A^{II}B^{VI}:3d^{2+}$ with a crystal structure of sphalerite: $ZnSe:Ni^{2+}$ [63], ZnSe: Cr^{2+} [64,65], $ZnSe:V^{2+}$ [66] , $ZnTe:Ni^{2+}$ [67] , and $ZnSe:Fe^{2+}$ [68]. As the results of these investigations, a more correct expression for relaxation time calculation was introduced which contained T_1 instead of T_m and the procedure of T_1 determining was introduced. Besides, the method of construction of temperature dependences of the relaxed (isothermal) and unrelaxed (adiabatic) moduli was developed.

The $A^{II}B^{VI}:3d^{2+}$ compounds contain the JT ion in tetrahedral coordination (see Figure 1.1). Investigation of the crystals with other JT complexes could be a natural extension of the JTE investigation in doped crystals by means of ultrasonic technique. The present dissertation is focused on the fluoride crystals with the JT center in 8-ions coordination. Attention was paid to the triply degenerate 3d dopants since in this case we can meet with a variety of the ground state symmetry properties. In advance, it is impossible to predict whether the global minima will be tetragonal (like in studied sphalerite crystals), trigonal or orthorhombic ones.

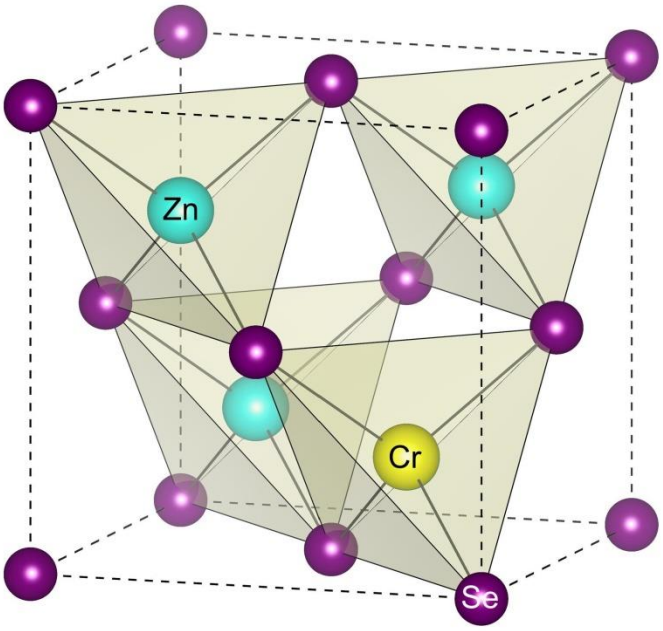

Figure 1.1 – A-substituted ZnSe:Cr with sphalerite (zinc-blend) crystal structure. Figure is reproduced from [69].

CHAPTER 2. THE CRYSRALS STUDIED AND EXPERIMENTAL THECHNIQUE

2.1. The crystals studied

The structure of fluorite type crystal $\left[Fm\bar{3}m\ (O_h^5)\right]$ is shown in Figure 2.1. Calcium ions occupy the positions with coordinates (0, 0, 0), (1/2, 1/2, 0), (1/2, 0, 1/2), and (0, 1/2, 1/2) while fluorine ions occupy the positions (3/4, 1/4, 1/4), (1/4, 3/4, 1/4), (1/4, 1/4, 3/4), (3/4, 3/4, 3/4), (1/4, 1/4, 1/4), (3/4, 3/4, 1/4), (1/4, 3/4, 3/4), and (3/4, 1/4, 3/4).

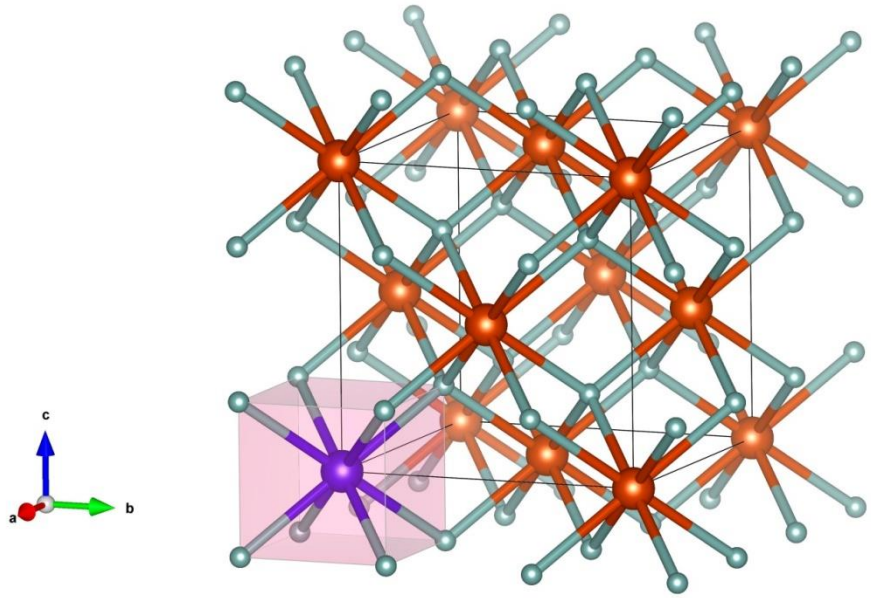

Figure 2.1 – A-substituted CaF_2:3*d* with fluorite crystal structure red are calcium ions, green are fluorine ions, blue is 3*d* substitution ion. The 3*d*F_8 complex is outlined by pink

The single crystal of **CaF_2** doped with **Cr^{2+}** was produced at the E.K. Zavoisky Physical-Technical Institute, Kazan Scientific Center of the RAS by the Czochralski method. The chromium ions were added to a melt in a form of carefully dehydrated chromium fluoride powders. To prepare the helium–fluorine atmosphere the fluorine gas was done by thermal decomposition of Teflon. This encouraged an increase of chromium concentration dissolved in the melt. It proved to be a necessary condition for incorporating chromium into the lattice of the

growing crystal [70]. Concentration of the dopant in this case and in all other studied crystals was measured at the Institute of Solid State Chemistry, Ural Branch of the RAS using ELAN 9000 ICP-MS quadruple-based instrument (Perkin-Elmer SCIEX).

In CaF_2 doped with Cr, concentration of the chromium ions proved to be $n = (4.74 \pm 0.03) \times 10^{19} \text{cm}^{-3}$. It significantly surpassed the concentration of other 3*d* metals. Since the mean distance between the Cr impurities is large, the JT centers can be treated as non-interacting ones. The nominally pure CaF_2 sample was crystallized by the Bridgman–Stockbarger method at the A.P. Vinogradov Institute of Geochemistry, Siberian Branch of the RAS. Concentration of 3*d* impurities in it was less than $9 \times 10^{17} \text{cm}^{-3}$. The result of XRD analysis of our CaF_2:Cr crystal done in Bregg–Brentano geometry with the step of 0.04 deg is presented in Figure 2.3. It shows that due to small concentration of the dopant the diffractogram of this crystal is almost identic to one of pure CaF_2. Chromium ion substitutes Ca^{2+} with eight fluorine ions as the nearest neighbors in the corners of the cube. In cubic coordination, Cr^{2+} ion has ground orbital triplet ${}^5T_{2g}\left(e_g^2 t_{2g}^2\right)$ (see Table 1 in [33]). However, an aliovalent substitution is also possible. Some papers report properties of Cr^{3+} ions in the fluorite-type matrix [71–73].

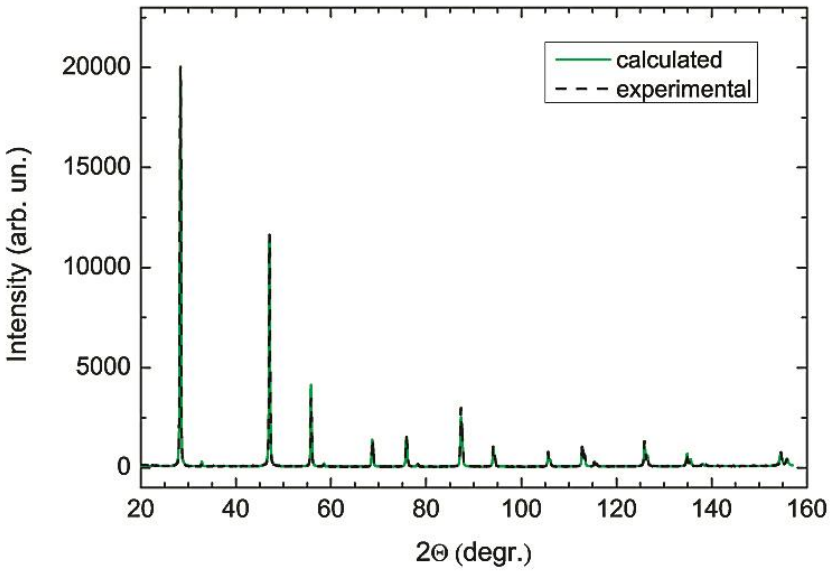

Figure 2.3 – X-ray diffractogram of the studied crystal CaF_2:Cr (dash curve) and theoretical one for CaF_2 (using the database http://crystallography.net) with account of background signal.

The single crystal of **SrF_2:Cr^{2+}** was grown at the E.K. Zavoisky Physical-Technical Institute, Kazan Scientific Center of the RAS by Czochralski technique in a helium atmosphere. Concentration of chromium ion $n = (1.60 \pm 0.03) \times 10^{19}\,\mathrm{cm}^{-3}$.

The crystal of **CaF_2** doped with **Ni^{2+}** ions was grown from the melt by the Bridgman-Stockbarger method in a helium atmosphere at the A.P. Vinogradov Institute of Geochemistry, Siberian Branch of the RAS. Before loading the mixture into the crucible, the salt of transition metal NiF_2 was dried in vacuum oven for several days. In the growth of alkaline earth fluorite single crystals, a small amount of CdF_2 is generally used as a scavenger in order to remove oxides and oxyfluorites contained in the raw materials by the reaction $CdF_2 + CaO \rightarrow CdO + CaF_2$. CdO and CdF_2 excess evaporate completely from the melt before crystallization begins. The Ni^{2+} ion in cubic coordination has ground orbital triplet ${}^3T_{1g}\left(e_g^4 t_{2g}^4\right)$ (see Table 1 in [33]).

The **CaF_2:Cu^{2+}** crystal was produced at the E.K. Zavoisky Physical–Technical Institute, Kazan Scientific Center of the RAS by the Czochralski technique which details are given in [74]. The copper ions concentration was

$n = (7.12 \pm 0.03) \times 10^{19} \text{cm}^{-3}$. In case of isovalent copper substitution of Ca^{2+}, a cubic JT complexes is formed leading to the orbital triply degenerate JT centers with the term $^2T_{2g}\left(e_g^4 t_{2g}^5\right)$ (see, e.g., Table 1 in [33]). Based on ESR data, it was established that at a concentration of copper ions no more than 0.5 at. % (the crystal under study falls into this category) mostly orthorhombic centers are formed [74], although it is well known that Cu^{2+} ions in crystals with the fluorite structure can arrange off-centers as well [75, 76].

In general case, the JT complex composed by JT center with the orbital triply degenerate ground state possesses the APES defined in 5 symmetrized coordinates $\left(Q_\vartheta, Q_\varepsilon, Q_\xi, Q_\eta, Q_\zeta\right)$ [38]. All the investigated JT complexes belong to this category.

2.2. The experimental technique

The experiments were carried out at the Ural Federal University using the setup which Block diagram is given in Figure 2.4. It operated as a frequency variable bridge [62]. It is based on a radio-pulse-echo method and square-wave frequency modulation for control of the signal phase. High frequency vibrations of the piezoelectric transducer 1 are excited by an electric signal which possesses the form of a radio pulse of about 1 μs. After passage through the specimen, the mechanical vibrations are transformed into an electric oscillations by the receiving piezoelectric transducer 2 placed on the opposite edge of the specimen. The received signal is amplified and mixed with the reference one of the same frequency. After integrating the resulting signals with gated box-car averager, the output direct current signal, is used for the frequency adjustment, keeping the phase constant $\varphi = kl = \varphi_0$ and for measuring the amplitude of the received radio pulses. Typical instrumental accuracy of the measurements of real and imaginary components of $\Delta k / k_0$ is about 10^{-6}. It is provided by the accuracy of 10 Hz for measuring the frequency of about 30 MHz and 1 mV for measuring the voltage of about 1 V.

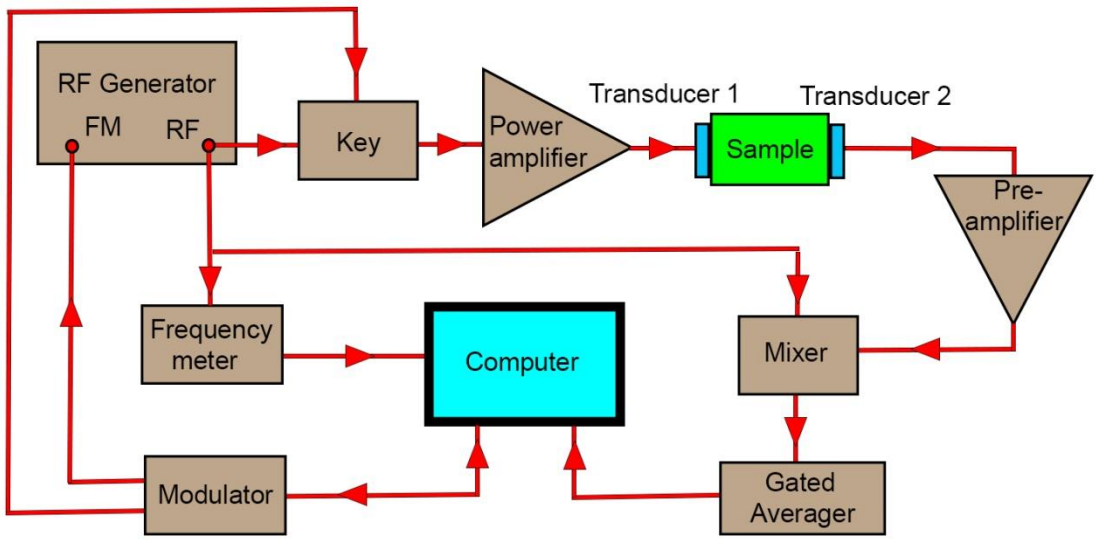

Figure 2.4 – Block diagram of the installation with frequency modulation of the signal

The measured values of $\Delta f / f_0$ and U / U_0 were converted to $\mathrm{Re}\,\Delta k / k_0$ and $\Delta\alpha$ with the use of equations (1.22) and (1.23).

CHAPTER 3. ADIABATIC POTENTIAL ENERGY SURFACE OF THE JAHN-TELLER COMPLEXES IN $SrF_2:Cr^{2+}$ CRYSRAL

3.1. Isothermal moduli of the subsystem formed by cubic JT complexes in a fluorite-type crystal

In Ref. [37], the results of ultrasonic investigations of the $SrF_2:Cr^{2+}$ crystal were published. First of all, the expressions for the contribution of the subsystem arranged by the cubic JT complexes to the isothermal moduli of a cubic crystal were introduced. It was shown that the expression of this contribution for a certain modulus depends upon the symmetry properties of the APES global minima. By means of measuring the temperature dependences of c_{44} and $c_E = (c_{11} - c_{12})/2$, one can solve this problem. We will reproduce here these expressions since it is important for our further consideration.

Table 3.1 – Isothermal contribution of the cubic JT complexes to the elastic moduli of a fluorite-type crystal. a_0 is the distance between the JT ion and the nearest neighbor (fluorine ion). After [37].

Symmetry properties of the APES minima	c_{11}^{JT}	c_{12}^{JT}	c_E^{JT}	c_{44}^{JT}
E	$-\frac{8}{27}\frac{na_0^2F_E^2}{k_BT}$	$\frac{4}{27}\frac{na_0^2F_E^2}{k_BT}$	$-\frac{2}{9}\frac{na_0^2F_E^2}{k_BT}$	0
T	0	0	0	$-\frac{16}{27}\frac{na_0^2F_T^2}{k_BT}$
OR	$-\frac{1}{54}\frac{na_0^2F_E^2}{k_BT}$	$-\frac{1}{108}\frac{na_0^2F_E^2}{k_BT}$	$-\frac{1}{72}\frac{na_0^2F_E^2}{k_BT}$	$-\frac{4}{9}\frac{na_0^2F_T^2}{k_BT}$

Dispersion and dissipation of the ultrasonic modes depend on the isothermal modulus with defines the order of the magnitude (see equation (1.21). Analyzing the Table 3.1, one can notice: the anomalies in real and imaginary parts of $c_{44}(T)$

and the absence of them in $c_E(T)$ indicate the trigonal symmetry of the global minima, the opposite case reveals tetragonal symmetry, and the presence of the anomalies in both the moduli justifies orthorhombic global minima. According to this approach, the APES global minima of the introduced $Cr^{2+}F_8$ complexes in SrF_2 crystal are orthorhombic ones. Here we will modify these expressions meaning that we have three JT subsystems: one has the JT complexes additionally (with respect to JTE) distorted along the x axis of the cube, the second one has the complexes additionally distorted along the y axis, and the complexes of the third subsystem are additionally distorted along the z axis. This modification will help us to interpret the results of the experiments discussed in chapter 5. Static additional deformation will be denoted with the superscript "0". The expressions for ΔE_k entering equation (1.15) have the following form for deformation ε_1^0 along the x axis:

$$\Delta E_1^{(1)} = -\frac{1}{4}F_E a\left(\varepsilon_1 + \varepsilon_1^0\right) + aF_T\left(\varepsilon_1 + \varepsilon_1^0 + \varepsilon_2 + \varepsilon_3 + \varepsilon_6\right), \tag{3.1}$$

$$\Delta E_2^{(1)} = -\frac{1}{4}F_E a\left(\varepsilon_1 + \varepsilon_1^0\right) + aF_T\left(\varepsilon_1 + \varepsilon_1^0 + \varepsilon_2 + \varepsilon_3 - \varepsilon_6\right), \tag{3.2}$$

$$\Delta E_3^{(1)} = -\frac{1}{4}F_E a\varepsilon_2 + aF_T\left(\varepsilon_1 + \varepsilon_1^0 + \varepsilon_2 + \varepsilon_3 + \varepsilon_5\right), \tag{3.3}$$

$$\Delta E_4^{(1)} = -\frac{1}{4}F_E a\varepsilon_2 + aF_T\left(\varepsilon_1 + \varepsilon_1^0 + \varepsilon_2 + \varepsilon_3 - \varepsilon_5\right), \tag{3.4}$$

$$\Delta E_5^{(1)} = -\frac{1}{4}F_E a\varepsilon_3 + aF_T\left(\varepsilon_1 + \varepsilon_1^0 + \varepsilon_2 + \varepsilon_3 + \varepsilon_4\right), \tag{3.5}$$

$$\Delta E_6^{(1)} = -\frac{1}{4}F_E a\varepsilon_3 + aF_T\left(\varepsilon_1 + \varepsilon_1^0 + \varepsilon_2 + \varepsilon_3 - \varepsilon_4\right), \tag{3.6}$$

for deformation ε_2^0 along the y axis:

$$\Delta E_1^{(2)} = -\frac{1}{4}F_E a\varepsilon_1 + aF_T\left(\varepsilon_1 + \varepsilon_2 + \varepsilon_2^0 + \varepsilon_3 + \varepsilon_6\right), \tag{3.7}$$

$$\Delta E_2^{(2)} = -\frac{1}{4}F_E a\varepsilon_1 + aF_T\left(\varepsilon_1 + \varepsilon_2 + \varepsilon_2^0 + \varepsilon_3 - \varepsilon_6\right), \tag{3.8}$$

$$\Delta E_3^{(2)} = -\frac{1}{4}F_E a\left(\varepsilon_2 + \varepsilon_2^0\right) + aF_T\left(\varepsilon_1 + \varepsilon_2 + \varepsilon_2^0 + \varepsilon_3 + \varepsilon_5\right), \tag{3.9}$$

$$\Delta E_4^{(2)} = -\frac{1}{4} F_E a\left(\varepsilon_2 + \varepsilon_2^0\right) + aF_T\left(\varepsilon_1 + \varepsilon_2 + \varepsilon_2^0 + \varepsilon_3 - \varepsilon_5\right), \tag{3.10}$$

$$\Delta E_5^{(2)} = -\frac{1}{4} F_E a\varepsilon_3 + aF_T\left(\varepsilon_1 + \varepsilon_2 + \varepsilon_2^0 + \varepsilon_3 + \varepsilon_4\right), \tag{3.11}$$

$$\Delta E_6^{(2)} = -\frac{1}{4} F_E a\varepsilon_3 + aF_T\left(\varepsilon_1 + \varepsilon_2 + \varepsilon_2^0 + \varepsilon_3 - \varepsilon_4\right), \tag{3.12}$$

and for deformation ε_3^0 along the z axis:

$$\Delta E_1^{(3)} = -\frac{1}{4} F_E a\varepsilon_1 + aF_T\left(\varepsilon_1 + \varepsilon_2 + \varepsilon_3 + \varepsilon_3^0 + \varepsilon_6\right), \tag{3.13}$$

$$\Delta E_2^{(3)} = -\frac{1}{4} F_E a\varepsilon_1 + aF_T\left(\varepsilon_1 + \varepsilon_2 + \varepsilon_3 + \varepsilon_3^0 - \varepsilon_6\right), \tag{3.14}$$

$$\Delta E_3^{(3)} = -\frac{1}{4} F_E a\varepsilon_2 + aF_T\left(\varepsilon_1 + \varepsilon_2 + \varepsilon_3 + \varepsilon_3^0 + \varepsilon_5\right), \tag{3.15}$$

$$\Delta E_4^{(3)} = -\frac{1}{4} F_E a\varepsilon_2 + aF_T\left(\varepsilon_1 + \varepsilon_2 + \varepsilon_3 + \varepsilon_3^0 - \varepsilon_5\right), \tag{3.16}$$

$$\Delta E_5^{(3)} = -\frac{1}{4} F_E a\left(\varepsilon_3 + \varepsilon_3^0\right) + aF_T\left(\varepsilon_1 + \varepsilon_2 + \varepsilon_3 + \varepsilon_3^0 + \varepsilon_4\right), \tag{3.17}$$

$$\Delta E_6^{(3)} = -\frac{1}{4} F_E a\left(\varepsilon_3 + \varepsilon_3^0\right) + aF_T\left(\varepsilon_1 + \varepsilon_2 + \varepsilon_3 + \varepsilon_3^0 - \varepsilon_4\right). \tag{3.18}$$

Here a is the edge of the cubic complex $Cr^{3+}F_8^-$.

Introducing $C = -F_E a / 4k_B T$ and $D = -F_T a / k_B T$, we have obtained the following expressions for the isothermal contributions of the JT subsystems to the total moduli of the crystal according to equations. (1.13)- (1.15):

$$c_{11}^{(1)} = -nk_B T\left\{-\frac{\left[\left(-C+D\right)e^{-C\varepsilon_1^0 + D\varepsilon_1^0} + 2De^{D\varepsilon_1^0}\right]^2}{\left[2e^{D\varepsilon_1^0} + e^{-C\varepsilon_1^0 + D\varepsilon_1^0}\right]^2} + \frac{\left(-C+D\right)^2 e^{-C\varepsilon_1^0 + D\varepsilon_1^0} + 2D^2 e^{D\varepsilon_1^0}}{2e^{D\varepsilon_1^0} + e^{-C\varepsilon_1^0 + D\varepsilon_1^0}}\right\}, \tag{3.19}$$

$$c_{11}^{(2)} = -nk_B T\left\{-\frac{\left[\left(-C+2D\right)e^{D\varepsilon_2^0} + De^{-C\varepsilon_2^0 + D\varepsilon_2^0}\right]^2}{\left[2e^{D\varepsilon_2^0} + e^{-C\varepsilon_2^0 + D\varepsilon_2^0}\right]^2} + \frac{\left[\left(-C+D\right)^2 + D^2\right]e^{D\varepsilon_2^0} + D^2 e^{-C\varepsilon_2^0 + D\varepsilon_2^0}}{2e^{D\varepsilon_2^0} + e^{-C\varepsilon_2^0 + D\varepsilon_2^0}}\right\},$$

(3.20)

$$c_{11}^{(3)} = -nk_B T\left\{-\frac{\left[\left(-C+2D\right)e^{D\varepsilon_3^0} + De^{-C\varepsilon_3^0 + D\varepsilon_3^0}\right]^2}{\left[2e^{D\varepsilon_3^0} + e^{-C\varepsilon_3^0 + D\varepsilon_3^0}\right]^2} + \frac{\left[\left(-C+D\right)^2 + D^2\right]e^{D\varepsilon_3^0} + D^2 e^{-C\varepsilon_3^0 + D\varepsilon_3^0}}{2e^{D\varepsilon_3^0} + e^{-C\varepsilon_3^0 + D\varepsilon_3^0}}\right\},$$

(3.21)

$$c_{12}^{(1)} = -nk_BT\left\{-\frac{\left[De^{-C\varepsilon_1^0+D\varepsilon_1^0}+\left(-C+2D\right)e^{D\varepsilon_1^0}\right]\times\left[\left(-C+D\right)e^{-C\varepsilon_1^0+D\varepsilon_1^0}+2De^{D\varepsilon_1^0}\right]}{\left[2e^{D\varepsilon_1^0}+e^{-C\varepsilon_1^0+D\varepsilon_1^0}\right]^2}+\frac{\left(-C+D\right)De^{-C\varepsilon_1^0+D\varepsilon_1^0}+\left(-C+2D\right)De^{D\varepsilon_1^0}}{2e^{D\varepsilon_1^0}+e^{-C\varepsilon_1^0+D\varepsilon_1^0}}\right\}, \tag{3.22}$$

$$c_{12}^{(2)} = -nk_BT\left\{-\frac{\left[2De^{D\varepsilon_2^0}+\left(-C+D\right)e^{-C\varepsilon_2^0+D\varepsilon_2^0}\right]\times\left[\left(-C+2D\right)e^{D\varepsilon_2^0}+De^{-C\varepsilon_2^0+D\varepsilon_2^0}\right]}{\left[2e^{D\varepsilon_2^0}+e^{-C\varepsilon_2^0+D\varepsilon_2^0}\right]^2}+\frac{\left(-C+2D\right)De^{D\varepsilon_2^0}+\left(-C+D\right)De^{-C\varepsilon_2^0+D\varepsilon_2^0}}{2e^{D\varepsilon_2^0}+e^{-C\varepsilon_2^0+D\varepsilon_2^0}}\right\}, \tag{3.23}$$

$$c_{12}^{(3)} = -nk_BT\left\{-\frac{\left[\left(-C+2D\right)e^{D\varepsilon_3^0}+De^{-C\varepsilon_3^0+D\varepsilon_3^0}\right]^2}{\left[2e^{D\varepsilon_3^0}+e^{-C\varepsilon_3^0+D\varepsilon_3^0}\right]^2}+\frac{2\left(-C+D\right)De^{D\varepsilon_3^0}+D^2e^{-C\varepsilon_3^0+D\varepsilon_3^0}}{2e^{D\varepsilon_3^0}+e^{-C\varepsilon_3^0+D\varepsilon_3^0}}\right\}, \tag{3.24}$$

$$c_{44}^{(1)} = -nk_BT\frac{D^2e^{D\varepsilon_1^0}}{2e^{D\varepsilon_1^0}+e^{-C\varepsilon_1^0+D\varepsilon_1^0}}, \tag{3.25}$$

$$c_{44}^{(2)} = -nk_BT\frac{D^2e^{D\varepsilon_2^0}}{2e^{D\varepsilon_2^0}+e^{-C\varepsilon_2^0+D\varepsilon_2^0}}, \tag{3.26}$$

$$c_{44}^{(3)} = -nk_BT\frac{D^2e^{-C\varepsilon_3^0+D\varepsilon_3^0}}{2e^{D\varepsilon_3^0}+e^{-C\varepsilon_3^0+D\varepsilon_3^0}}. \tag{3.27}$$

In equations (3.1) – (3.27), the superscripts $i=1,\ 2,\ 3$ indicate the axes $x,\ y,\ z$, respectively, along which the static deformations ε_i^0 take place. As a result, we can conclude the isothermal JT contribution to all the elastic moduli in a cubic crystal depends on both tetragonal and trigonal linear vibronic coupling constants if the complex undergoes additional static deformation along at least one of the cubic axes. In other word, the additional deformations substantially level the manifestation of the JTE in different normal modes. In the case of SrF_2:Cr^{2+}, anomalies in $c_{44}(T)$ were significantly larger ones in $c_E(T)$. According to the Table 3.1, it justifies the orthorhombic APES global minima.

3.2. Temperature dependence of relaxation time

Temperature dependence of relaxation time of the JT subsystem can be constructed with the use of temperature dependence of ultrasonic attenuation $\Delta\alpha_\beta(T)$ and extraction of background attenuation $\Delta\alpha_\beta^b(T)$. Sturge [33] discussed

three mechanisms of relaxation while interpreting the experimental data: thermal activation (τ_a), tunneling (τ_t), and two-phonon (τ_R) ones:

$$\tau_a = \tau_0 \exp(V_0 / T), \tag{3.28}$$

$$\tau_t = \left(BT\right)^{-1}, \tag{3.29}$$

$$\tau_R = \left[\left(B/\Theta^2\right)T^3\right]^{-1}, \tag{3.30}$$

where V_0 is activation energy, τ_0^{-1} is frequency of attempts, B and Θ are constants of $s^{-1}K^{-1}$ and K dimensions, respectively. Equation (1.21) written for attenuation in high-frequency limit $\omega\tau \gg 1$ which means low temperature limit as well, has the form of

$$\left(\frac{\alpha_\beta^{JT}}{k_0}\right)_{\omega\tau\to\infty} = \frac{1}{2}\frac{\left(c_\beta^{JT}\right)^T}{c_0}\frac{\tau^{-1}}{\omega}. \tag{3.31}$$

Since $(c_\beta^{JT})^T \propto T^{-1}$ (see Table 3.1.) and $\tau_t^{-1} \propto T$ (equation (3.29), the right hand part of equation (3.31) is a non-vanishing constant value. In general case, this value is important when one constructs the temperature dependence of the background attenuation $\alpha_\beta^b(T)$. However, the peak of relaxation attenuation located at considerably high temperature ($T > 40$ K) justifies large relaxation time and small value of relaxation rate at low temperatures. This is the case observed in the SrF_2:Cr^{2+} crystal (see Figures. 3.1 and 3.2).

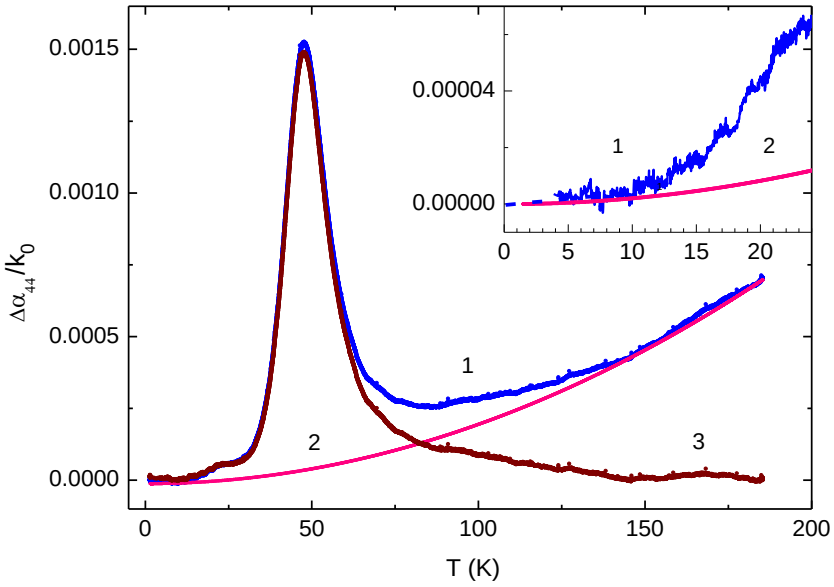

Figure 3.1 – Temperature dependence of ultrasonic attenuation in the $SrF_2:Cr^{2+}$ crystal. The c_{44} mode at 105 MHz (curve 1) $\Delta\alpha_{44}/k_0 = \left[\alpha_{44}(T) - \alpha_{44}(T \to 0)\right]/k_0$, the background attenuation $\alpha_{44}^b(T) = 2.07 \cdot 10^{-8} T^{-2}$ (2), and contribution of the JT subsystem $\alpha_{44}^{JT}/k_0 = \left[\Delta\alpha_{44}^{JT}(T) - \alpha_{44}^b(T)\right]/k_0$ (3). After [37].

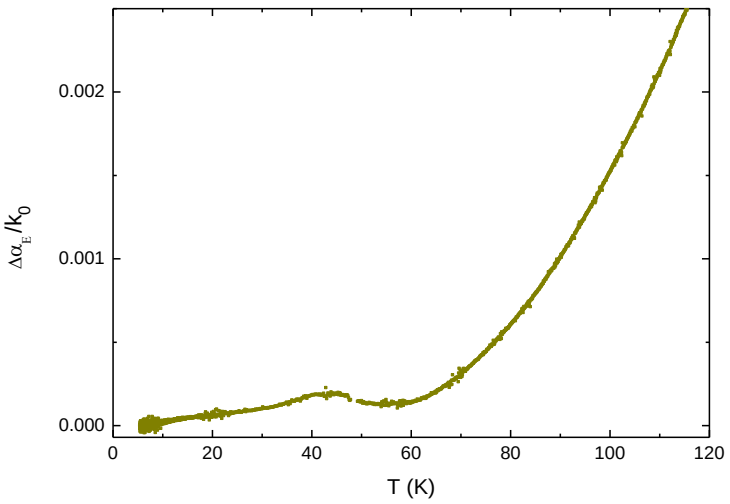

Figure 3.2 – Temperature dependence of ultrasonic attenuation in the SrF2:Cr^{2+} crystal. The c_E mode at 56 MHz.

Therefore, we can formulate the requirement for $\alpha_\beta^b(T)$ construction: it should coincide with the measured dependence $\Delta a_\beta(T)$ at low ($T \ll T_1$) and high ($T \gg T_1$) temperatures. Here the temperature T_1 is introduced which corresponds to the

condition $\omega\cdot\tau(T_1)=1$. In Figure 3.1 the dependence of $\alpha_{44}^{b}(T)=2.07\cdot10^{-8}T^{-2}$ matches the mentioned requirements. So, the JT contribution to ultrasonic attenuation obtained in an experiment can be introduced as

$$\alpha_{\beta}^{JT}=\Delta\alpha_{\beta}(T)-\alpha_{\beta}^{b}(T)\,. \tag{3.32}$$

The precise magnitude of T_1 can be determined with the use of the temperature dependence of the product $\alpha_{\beta}^{JT}(T)\cdot T$. Multiplying $\alpha_{\beta}^{JT}(T)$ by T eliminates the inverse temperature dependence of attenuation (initiated by the isothermal modulus) and the product is proportional to $\omega\tau/\left[1+(\omega\tau)^2\right]$. Maximum of $\alpha_{\beta}^{JT}(T)\cdot T$ occurs at $T=T_1$. Such procedure is shown in Figure 3.3. In the narrow temperature interval, the peak can be simulated with a parabola $f=a-b\cdot(T-T_1)^2$.

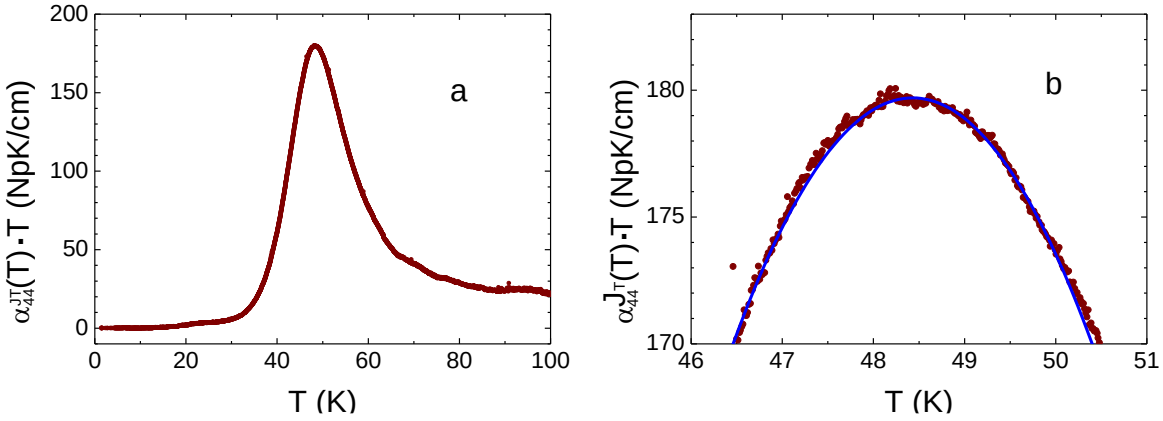

Figure 3.3 – Temperature dependence of $\alpha_{44}^{JT}(T)\cdot T$ at 105 MHz (symbols) and model curve $f=179.7-2.5\cdot(T-48.43)^2$.

In our case, $a=179.7$ (Np/cm)·K, $T_1=48.43$ K. The value of $a=\alpha_{\beta}^{JT}(T_1)\cdot T^1$ is also will be used below for evaluation of relaxation time temperature dependence.

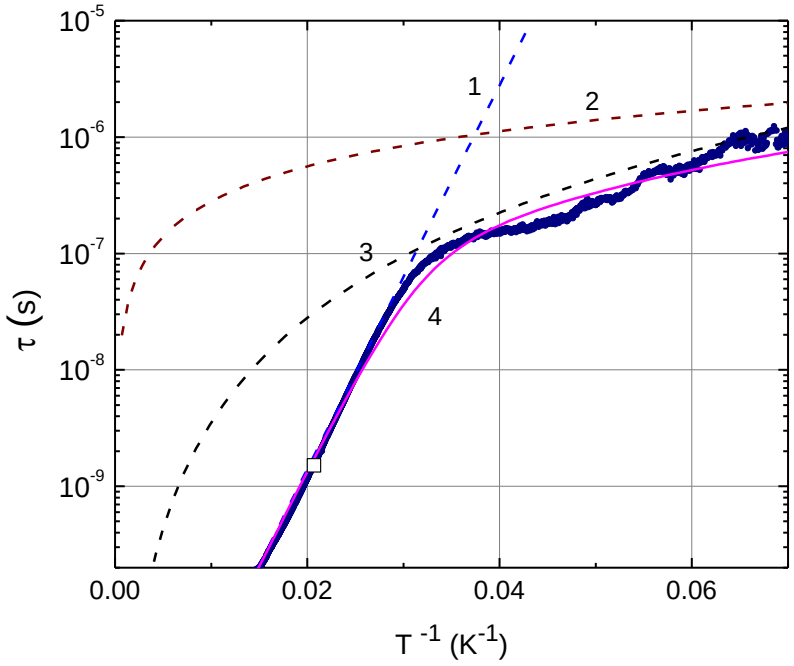

Figure 3.4 –Temperature dependence of relaxation time in SrF_2:Cr^{2+} crystal determined with the use of the data given in Figure 3.1. Dark solid line is experimental data, curve 1 is activation relaxation time $\tau_a = 7\cdot10^{-13}\exp(380/T)$, curve 2 is tunneling relaxation time $\tau_t = 2.8\cdot10^{-5}T^{-1}$, curve 3 is relaxation time due to two-phonon mechanism $\tau_R = 3.5\cdot10^{-3}T^{-3}$, curve 4 is total relaxation time $\tau = \left(\tau_a^{-1} + \tau_t^{-1} + \tau_R^{-1}\right)^{-1}$. The square symbol corresponds to $\omega\tau(T) = 1$.

For calculation of the temperature dependence of relaxation time we can use the expression (see , e.g., [60])

$$\tau(T) = \frac{1}{\omega}\left\{\frac{\alpha_\beta^{JT}(T_1)\cdot T_1}{\alpha_\beta^{JT}(T)\cdot T} \pm \sqrt{\left[\frac{\alpha_\beta^{JT}(T_1)\cdot T_1}{\alpha_\beta^{JT}(T)\cdot T}\right]^2 - 1}\right\}. \qquad (3.33)$$

In [37] the dependence $\tau(1/T)$ was interpreted as one revealing two activation mechanisms: $\tau^{(1)} = 5\cdot10^{-11}\exp(390/T)$ (high temperature range) and $\tau^{(1)} = 5\cdot10^{-9}\exp(65/T)$ (low temperatures). Such approach contains an ambiguity in choice of V_0, the parameter determining the magnitude of the potential energy barrier and the JT stabilization energy. Meaning high importance of this parameter, we applied the approach used by Sturge [33] and completed the fitting of the experimental curve

$\tau(1/T)$ with the help of the mechanisms given by equations (3.28)-(3.30). The result of such fitting is shown in Figure 3.4. It proved to be that $V_0 = 380$ K simulates well the experimental curve and we will use this magnitude in our further calculation of the APES parameters.

3.3. Parameters of the adiabatic potential energy surface

The orthorhombic APES global minima in the SrF_2:Cr^{2+} crystal, justified in paragraph 3.1, indicate the quadratic $T \otimes (e + t_2)$ JTE problem (see, e.g., [38]. In this case, the depth of the saddle points is determined from the value of tetragonal (E^E) and trigonal (E^T) JT stabilization energies as follows [38]:

$$E^E = \frac{1}{2}\frac{F_E^2}{K_E}, \tag{3.34}$$

$$E^T = \frac{2}{3}\frac{F_T^2}{K_T}, \tag{3.35}$$

where, K_E and K_T are tetragonal and trigonal primary force constants. The expressions for calculation the linear vibronic coupling constants are obtained with the use of equation (1.21), written for $T = T_1$ and accounting $(c_\beta^{JT})^T$ given in Table 3.1.

$$F_E^2 = 288\frac{c_0 k_B}{n a_0^2}\frac{\alpha_E^{JT}(T_1)\cdot T_1}{k_0}, \tag{3.36}$$

$$F_T^2 = 9\frac{c_0 k_B}{n a_0^2}\frac{\alpha_T^{JT}(T_1)\cdot T_1}{k_0}, \tag{3.37}$$

In F_E^2 and F_T^2 calculations, the magnitude of $a_0 = 2.54$ Å was used. The JT stabilization energy for orthorhombic minima (i.e., the depth of the global minima of the APES) is determined by

$$E^{OR} = E^T + V_0 + \frac{1}{2}\hbar\omega_R, \tag{3.38}$$

where ω_R is the radial vibronic frequency. It can be accepted as equal to local trigonal-type vibrational frequency ω_τ. In our calculation, we used $\omega_R = 100$ cm^{-1}

as in [37]. The force constant K_T is defined by the product of ω_R^2 and the reduced mass of the CrF_8 complex $M = (m_{Cr} : 8m_F) \ / \ (m_{Cr} + 8m_F) = 6.43 \cdot 10^{-23}$g. The ratio of the primary force constants should match the relation between corresponding symmetry elastic moduli

$$\frac{K_E}{K_T} = \left(\frac{c_{11} - c_{12}}{2} \right) / c_{44} . \tag{3.39}$$

In our crystal, $c_{11} = 12.87 \cdot 10^{11}$ dyn/cm^2, $c_{12} = 4.7 \cdot 10^{11}$ dyn/cm, $c_{44} = 3.308 \cdot 10^{11}$ dyn/cm^2 $K_E / K_T = 0.815$. As a result, $K_T = 1.85 \cdot 10^4$ dyn/cm and $K_E = 2.29 \cdot 10^4$ dyn/cm.

Positions of orthorhombic global minima can be calculated introducing the dimensionless parameters [11]

$$A = \frac{W_{ET}}{\sqrt{K_E K_T}} \ , \tag{3.40}$$

$$B = \frac{W_{ET} F_E}{K_E K_T} , \tag{3.41}$$

where W_{ET} is the quadratic vibronic coupling constant. Obviously,

$$W_{ET} = A \sqrt{K_E K_T} \ , \tag{3.42}$$

$$\frac{A}{B} = \frac{\sqrt{K_E K_T}}{F_E} \ . \tag{3.43}$$

The values of A are defined by the quadratic equation

$$\frac{E_{OR}}{E_E} = \frac{(A/B)^2 - (A/B) A + 1/4}{(1 - A^2)} . \tag{3.44}$$

After calculation of A, B is derived from equation (3.43). Positions of the first orthorhombic minimum is defined as follows

$$Q_1^{OR} = \left(-\frac{F_E\left(B-2A^2\right)}{2K_E B\left(1-A^2\right)}, 0, 0, 0, -\frac{F_T\left(2-B\right)}{2K_T\left(1-A^2\right)} \right) . \qquad (3.45)$$

The other five minima can be obtained according to the Table 3.2. Coordinates of the saddle points are given in Tables 3.3 and 3.4. Numerical data which characterize the JTE and the APES in SrF_2:Cr^{2+} obtained in our study are given in Tables 3.5 and 3.6.

Table 3.2 – Positions of six orthorhombic minima in coordinates $\left(Q_\vartheta, Q_\varepsilon, Q_\xi, Q_\eta, Q_\zeta\right)$.

	Q_ϑ	Q_ε	Q_ξ	Q_η	Q_ζ
Q_1^{OR}	$Q_{0\vartheta}^{OR}$	0	0	0	$Q_{0\zeta}^{OR}$
Q_2^{OR}	$Q_{0\vartheta}^{OR}$	0	0	0	$-Q_{0\zeta}^{OR}$
Q_3^{OR}	$-\frac{1}{2}Q_{0\vartheta}^{OR}$	$\frac{\sqrt{3}}{2}Q_{0\vartheta}^{OR}$	0	$Q_{0\zeta}^{OR}$	0
Q_4^{OR}	$-\frac{1}{2}Q_{0\vartheta}^{OR}$	$\frac{\sqrt{3}}{2}Q_{0\vartheta}^{OR}$	0	$-Q_{0\zeta}^{OR}$	0
Q_5^{OR}	$-\frac{1}{2}Q_{0\vartheta}^{OR}$	$-\frac{\sqrt{3}}{2}Q_{0\vartheta}^{OR}$	$Q_{0\zeta}^{OR}$	0	0
Q_6^{OR}	$-\frac{1}{2}Q_{0\vartheta}^{OR}$	$-\frac{\sqrt{3}}{2}Q_{0\vartheta}^{OR}$	$-Q_{0\zeta}^{OR}$	0	0

Table 3.3 – Positions of three tetragonal saddle points in coordinates $\left(Q_\vartheta, Q_\varepsilon, Q_\xi, Q_\eta, Q_\zeta\right)$. $Q_0^E = F_E / K_E$

$\mathbf{Q}_1^E$	$\mathbf{Q}_2^E$	$\mathbf{Q}_2^E$
$Q_0^E\left(1,0,0,0,0\right)$	$Q_0^E\left(-\frac{1}{2},\frac{\sqrt{3}}{2},0,0,0\right)$	$Q_0^E\left(-\frac{1}{2},-\frac{\sqrt{3}}{2},0,0,0\right)$

Table 3.4 – Positions of four trigonal saddle points in coordinates $\left(Q_\vartheta, Q_\varepsilon, Q_\xi, Q_\eta, Q_\zeta\right)$. $Q_0^T = 2F_T / (3K_T)$

$\mathbf{Q}_1^T$	$\mathbf{Q}_2^T$	$\mathbf{Q}_3^T$	$\mathbf{Q}_4^T$
$Q_0^T(0,0,1,1,1)$	$Q_0^T(0,0,-1,1,-1)$	$Q_0^T(0,0,1,-1,-1)$	$Q_0^T(0,0,-1,-1,1)$

Table 3.5 – Stabilization energies for tetragonal, trigonal and orthorhombic APES extrema.

E_E, cm^{-1}	E_T, cm^{-1}	E_{OR}, cm^{-1}
225	440	754

Table 3.6 – Vibronic coupling constants and parameters $Q_{0\vartheta}^{OR}$, $Q_{0\zeta}^{OR}$, Q_0^E and Q_0^T entering Tables 3.2–3.4. Two magnitudes of W_{ET}, $Q_{0\vartheta}^{OR}$, $Q_{0\zeta}^{OR}$ for one set of (F_E, F_T) originate from two solutions of the quadratic equation (3.44) with respect to A.

F_E, dyn	F_T, dyn	W_{ET}, dyn/cm	Q_0^E, Å	Q_0^T, Å	$Q_{0\vartheta}^{OR}$, Å	$Q_{0\zeta}^{OR}$, Å
$5.3\cdot10^{-5}$	$5.5\cdot10^{-5}$	$-1.3\cdot10^4$	0.19	0.16	-0.17	0.41
		$2.3\cdot10^4$			1.0	0.83
$-5.3\cdot10^{-5}$	$-5.5\cdot10^{-5}$	$-1.3\cdot10^4$	-0.19	-0.16	0.17	-0.41
		$2.3\cdot10^4$			-1.0	-0.83
$5.3\cdot10^{-5}$	$-5.5\cdot10^{-5}$	$-1.3\cdot10^4$	0.19	-0.16	1.00	-0.83
		$2.3\cdot10^4$			-0.17	-0.41
$-5.3\cdot10^{-5}$	$5.5\cdot10^{-5}$	$-1.3\cdot10^4$	-0.19	0.16	-1.00	0.83
		$2.3\cdot10^4$			0.17	0.41

3.4. Conclusion

1. We have considered a cubic JT complex and have derived the expressions for its energy shifted by the additional static deformations.

2. Analyzing the experimental result obtained in SrF_2:Cr^{2+} single crystal we came to the conclusion that the additional static deformations are negligible in this case.

3. The anomaly which was observed in the temperature dependence of attenuation in SrF_2:Cr^2 was interpreted as due to relaxation in the subsystem of the JT complexes $Cr^{2+}F_8^-$ subject to the $T_{2g}\otimes\left(e_g+t_{2g}\right)$ JTE problem.

4. The temperature dependence of relaxation time was obtained and simulated with account of three mechanisms. The simulation pointed out the more accurate value of the activation energy with respect to published in [37].

5. Consequently, the magnitudes of the APES global minima, quadratic vibronic coupling constants, and positions of the extrema points (orthorhombic minima and trigonal and tetragonal saddle points) were calculated more accurately.

CHAPTER 4. ADIABATIC POTENTIAL ENERGY SURFACE OF THE JAHN-TELLER COMPLEXES IN $CaF_2:Ni^{2+}$ CRYSRAL

4.1. Temperature dependence of attenuation

The c_{44} and c_E modes revealed peak which was well described by the equation (1.21), as it is shown in Figure 4.1. Figure 4.1a shows the results of the experiment for two c_{44} modes measured at 17 and 52 MHz: a typical temperature shift of the relaxation peak caused by frequency reduction of the wave is clearly seen.

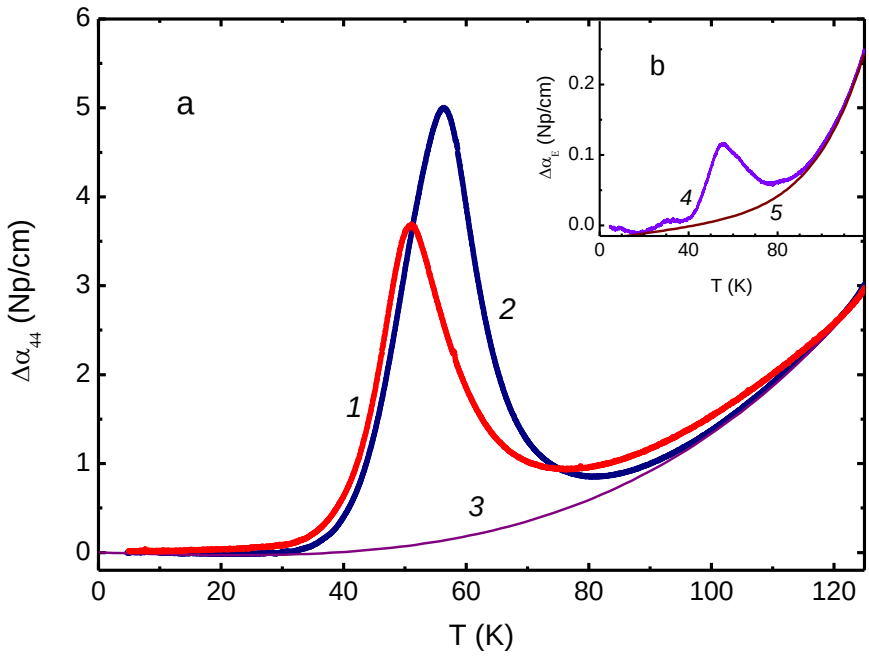

Figure 4.1 – Temperature dependences of ultrasonic attenuation: (a) c_{44} mode measured at 17 and 53 MHz (curves 1 and 2, respectively), (b) $(c_{11}-c_{12})/2$ E- mode at 54 MHz (4). Background attenuation is

$$\alpha_T^b = 4.32\cdot10^{-4} - 2\cdot10^{-3}\cdot T + 1.19\cdot10^{-6}\cdot T^3 + 3.45\cdot10^{-9}\cdot T^4 \quad (3) \text{ and}$$

$$\alpha_E^b = -0.02 + 4.2\cdot10^{-4}\times T + 2.19381\cdot10^{-8}\cdot T^3 + 10^{-11}\cdot T^4 + 1.1\cdot10^{-15}\times T^5 + 6.135\cdot10^{-14}\cdot T^6 \quad (5).$$

$$\Delta\alpha_\beta = \alpha_\beta(T) - \alpha_\beta(T_0),\ T_0 = 5\text{ K},\ \beta = 44,\ E\ .$$

Anomalies in both c_{44} and c_E modes, according to Table 3.1, indicate the orthorhombic symmetry of the APES global minima. It can be only in the case of

the quadratic $T \otimes (e + t_2)$ JTE problem as it was emphasized before. To obtain the JT contribution to the elastic moduli according to equation (3.32), we follow the approach given in paragraph 3.2: the background attenuation should coincide with the measured dependence $\Delta a_\beta(T)$ at low ($T \ll T_1$) and high ($T \gg T_1$) temperatures (remind, T_1 was introduced as corresponding to the condition $\omega\tau = 1$). As it can be seen in Figure 4.1, the following expressions match well to this requirement:

$$\alpha_T^b = 4.32 \cdot 10^{-4} - 2 \cdot 10^{-3} \cdot T + 1.19 \cdot 10^{-6} \cdot T^3 + 3.45 \cdot 10^{-9} \cdot T^4, \quad (4.1)$$

$$\alpha_E^b = -0.02 + 4.2 \cdot 10^{-4} \times T + 2.19381 \cdot 10^{-8} \cdot T^3 + \\ + 10^{-11} \cdot T^4 + 1.1 \cdot 10^{-15} \times T^5 + 6.135 \cdot 10^{-14} \cdot T^6. \quad (4.2)$$

4.2. Temperature dependence of relaxation time

The $\tau(T)$ dependence was calculated with the use of the data on $\Delta\alpha_{44}(T)$ for 53 MHz given in Figure 4.1a and equations (3.32), (3.33), and (4.1). The obtained dependence $\tau(T^{-1})$ is well simulated by the mentioned above mechanisms of relaxation (see Figure 4.2a) although the parameters which characterize the mechanisms are different in comparison with the discussed in the previous chapter.

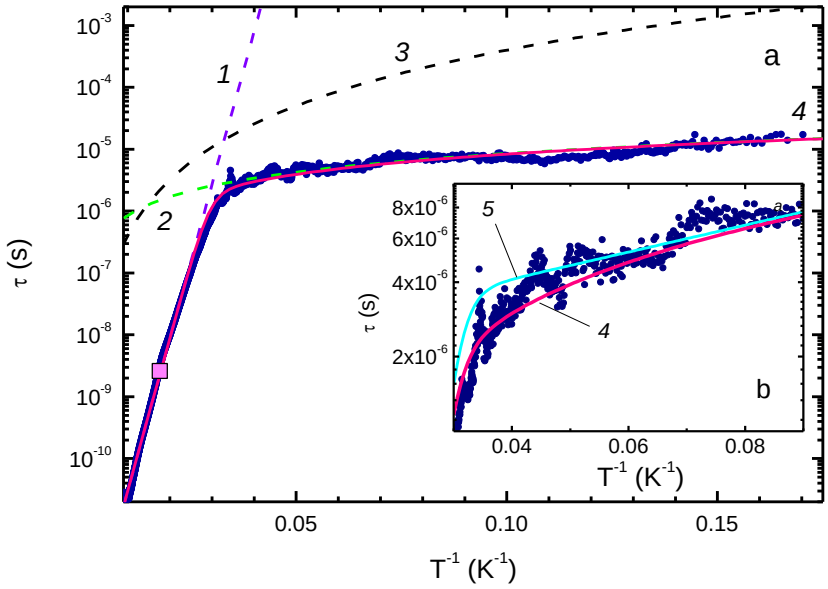

Figure 4.2 – Temperature dependence of relaxation time determined with the use of the data given in Figure 4.1 (curves 2 and 3). Dark circles are experimental data, curve 1 is activation relaxation time $\tau_a = 10^{-13}\exp(570/T)$, curve 2 is tunneling relaxation time $\tau_t = 8.5\cdot10^{-5}T^{-1}$, curve 3 is relaxation time due to two-phonon mechanism $\tau_R = 0.4\cdot T^{-3}$, curve 4 is $\tau = \left(\tau_a^{-1}+\tau_t^{-1}+\tau_R^{-1}\right)^{-1}$. Curve 5 represents another variant of fitting, namely, with two activation mechanisms $\tau=\{(10^{-13}\exp(570/T))^{-1}+[2.5\cdot10^{-6}\exp(12.5/T)]^{-1}\}^{-1}$

An attempt to simulate the dependence $\tau(T^{-1})$ with the help of two activation-type mechanisms was performed (see curve 5 in Figure 4.2b). Such simulation was done for $SrF_2:Cr^{2+}$ in [37]. In the previous chapter we showed that three-mechanisms simulation is more appropriate. In the crystal discussed in this chapter, we can state the same: the approach, which takes into account the activation and tunneling mechanisms, results in a more smooth curve and is in a better agreement with the experimental data.

4.3. Parameters of the adiabatic potential energy surface

Reproducing the procedure described by equations (3.34)-(3.45) with the following magnitudes of the entering constants: $\omega_R = 145\ \text{cm}^{-1}$ [79],

$(c_{11}-c_{12})/2 = 5.9\cdot10^{11}$ dyn/cm^2, $c_{44} = 3.58\cdot10^{11}$ dyn/cm^2, $K_T = 5.28\cdot10^4$ dyn/cm $K_E = 8.71\cdot10^4$ dyn/cm, and $a_0 = (\sqrt{3}/4)\cdot a$, and the lattice parameter $a = 5.46$ Å, we obtain the magnitudes of the vibronic coupling constants and the APES parameters presented in Tables 4.1 and 4.2.

Table 4.1 – Stabilization energies for tetragonal, trigonal and orthorhombic APES extrema.

E_E, cm^{-1}	E_T, cm^{-1}	E_{OR}, cm^{-1}
350	880	1290

Table 4.2 – Vibronic coupling constants and parameters $Q_{0\vartheta}^{OR}$, $Q_{0\zeta}^{OR}$, Q_0^E and Q_0^T entering Tables 3.2–3.4. Two magnitudes of W_{ET}, $Q_{0\vartheta}^{OR}$, $Q_{0\zeta}^{OR}$ for one set of (F_E, F_T) originate from two solutions of the quadratic equation (3.44) with respect to A

F_E, dyn	F_T, dyn	W_{ET}, dyn/cm	Q_0^E, Å	Q_0^T, Å	$Q_{0\vartheta}^{OR}$, Å	$Q_{0\zeta}^{OR}$, Å
$1.9\cdot10^{-4}$	$1.2\cdot10^{-4}$	$-3.3\cdot10^4$	0.125	0.15	-0.20	0.35
		$5.9\cdot10^4$			0.35	0.59
$-1.9\cdot10^{-4}$	$-1.2\cdot10^{-4}$	$-5.9\cdot10^4$	-0.125	-0.15	0.20	-0.35
		$3.3\cdot10^4$			-0.35	-0.59
$1.9\cdot10^{-4}$	$-1.2\cdot10^{-4}$	$-3.3\cdot10^4$	0.125	-0.15	0.35	-0.59
		$5.9\cdot10^4$			-0.20	-0.35
$-1.9\cdot10^{-4}$	$1.2\cdot10^{-4}$	$-3.3\cdot10^4$	-0.125	0.15	-0.35	0.59
		$5.9\cdot10^4$			0.20	0.35

One can see that the $Ni^{2+}F_8^-$ complexes in CaF_2 have larger magnitudes of the vibronic coupling constants and deeper extrema of the APES than $Cr^{2+}F_8^-$

complexes in SrF_2 matrix. What is the reason of these distinctions: different matrices or different ions? To clarify the situation we have competed the investigation of the same ion Cr^{2+} as in SrF_2 but in another matrix, namely, CaF_2. At the same time it was investigation of another ion (with respect to Ni^{2+}) but in the same matrix CaF_2.

4.4. Conclusion

1. Manifestation of the JTE in CaF_2:Ni^{2+} single crystal proved to be similar to one in SrF_2:Cr^{2+}, although the JT ions and host crystals are different.

2. In both the crystals, APES obeys orthorhombic global minima and subject to the quadratic $T \otimes (e + t_2)$ JTE problem, the relaxation attenuation peak was observed at relatively high temperatures (approximately 56 and 44 K at about 55 MHz, respectively).

3. Higher temperature of the peak location means lower relaxation time and higher potential energy barrier (or activation energy provided that the vibronic frequency is the same). Comparison of the activation energies reveals confirmation of this statement: V_0 = 570 and 380 K, respectively.

4. Besides, the $Ni^{2+}F_8^-$ complexes in CaF_2 have larger magnitudes of the vibronic coupling constants and deeper extrema of the APES than $Cr^{2+}F_8^-$ complexes in SrF_2 matrix.

CHAPTER 5. ADIABATIC POTENTIAL ENERGY SURFACE OF THE JAHN-TELLER COMPLEXES IN $CaF_2:Cr^{2+}$ CRYSRAL

5.1. Temperature dependence of attenuation

Figures 5.1 and 5.2 show the temperature dependences of the c_{44} and $c_L = c_{44} + (c_{11} + c_{12})/2$ modes. A distinctive feature of the curves shown in this Figure with respect to ones in Figures (3.1), (3.2), and (4.1), which present $\Delta\alpha_\beta(T)$ for $SrF_2:Cr^{2+}$ and $CaF_2:Ni^{2+}$, is considerably lower position of the relaxation peak in *T*-scale (8.7 K at 54 MHz) and, what is also important, the dependences do not reach their asymptotic low temperature limit.

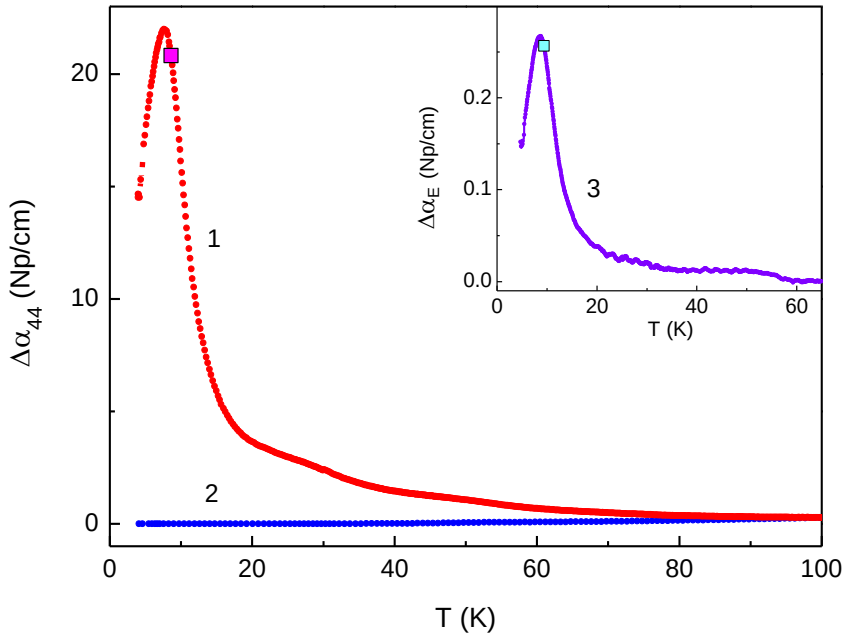

Figure 5.1 – Temperature dependence of attenuation coefficient of ultrasonic transverse wave associated with the trigonal modulus c_{44} measured at $\omega/2\pi$ = 39 MHz in CaF_2:Cr (curve 1) and in nominally pure CaF_2 (curve 2, $\omega/2\pi$ = 56 MHz). The reference temperature $T_0 = 100$ K for both the dependences. In the inset, curve 3 represents the temperature dependence of attenuation coefficient of transverse wave associated with the tetragonal modulus $c_E = (c_{11} - c_{12})/2$ measured at $\omega/2\pi$ = 55 MHz in CaF_2:Cr; $\Delta\alpha_\beta = \alpha_\beta(T) - \alpha_\beta(T_0)$, β = 44 or *E*, $T_0 = 65$ K. The square symbols correspond to the condition $\omega\tau = 1$.

This circumstance clearly points out higher than in the previous crystals relaxation rate (which means as well lower potential energy barriers). In essence, it means that we face the situation with noticeable magnitude of the low temperature limit of attenuation. In this case, the condition $\Delta a_\beta(T \to 0) = a_\beta^b(T \to 0)$ used above for determining the JT contribution $\alpha_\beta^{JT}(T)$ is not correct. Therefore we should apply a new approach for $\alpha_\beta^b(T)$ determination. Common feature of the JTE manifestation in all the studied crystals is observation of the peak in c_{44} and c_E modes (and besides in and c_L also) indicating the same orthorhombic global minima of the APES and the $T \otimes (e + t_2)$ JTE problem of the $Cr^{2+}F_8^-$ complexes in CaF_2 matrix.

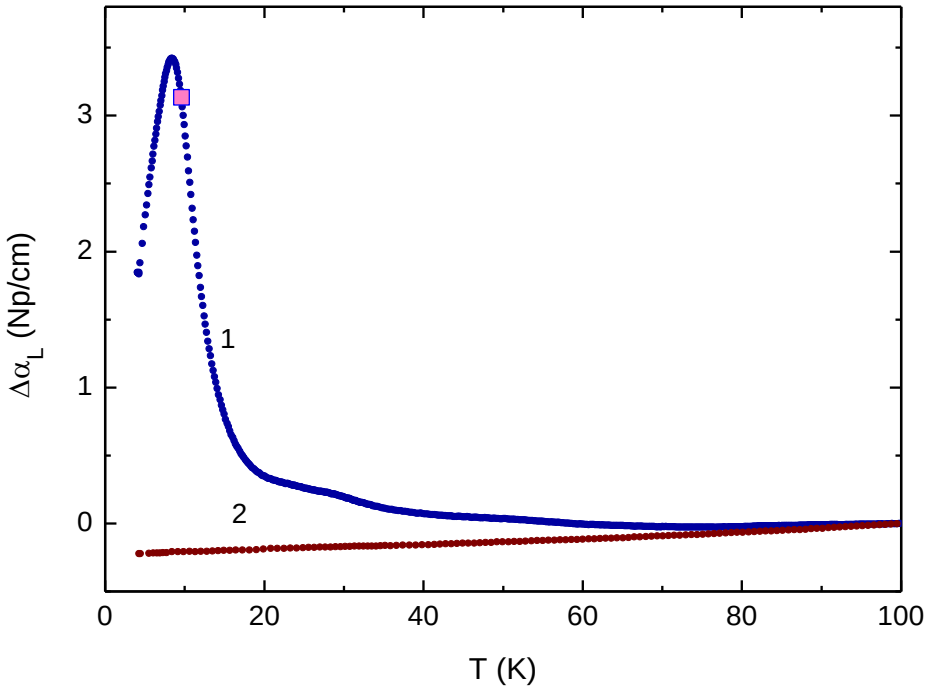

Figure 5.2 – Temperature dependence of attenuation coefficient of ultrasonic longitudinal wave associated with the modulus $c_L = c_{44} + (c_{11} + c_{12})/2$ measured in CaF_2:Cr (curve 1) and in nominally pure CaF_2 (curve 2). Wave vector $\mathbf{k}_L$ is parallel to the [110] crystallographic axis. $\omega/2\pi$ = 54 MHz, $\Delta\alpha_L = \alpha_L(T) - \alpha_L(T_0)$, $T_0 = 100$ K. The square symbol corresponds to the condition $\omega\tau = 1$.

5.2. JT contribution to the elastic moduli

In chapter 4, the following requirement for $\alpha_\beta^b(T)$ was formulated. First: it should coincide with the measured dependence $\Delta a_\beta(T)$ at low ($T \ll T_1$) and high ($T \gg T_1$). Second: the isothermal moduli have the inverse temperature dependence of the isothermal moduli as it can be seen in Table 3.1. This statement is correct irrespectively to the position of the relaxation peak in *T*-scale. We will use it here. Besides, we will use the proposition that the background attenuation is equal to attenuation of the waves in the nominally pure crystal shown by the curves 2 in Figures. 5.1 and 5.2. Therefore, the curves were presented so that the dependences $\Delta a_\beta(T)$ and $\alpha_\beta^b(T)$ do coincide at $T \geq T_0 = 100\ \mathrm{K}$ and the JT contributions are $\alpha_\beta^{JT} = \Delta\alpha_\beta(T) - \alpha_\beta^b(T)$, where $\alpha_\beta^b(T)$ are the curves corresponding to the nominally pure crystal (here $\beta = E, 44, L$). In the previous chapters we discussed the c_{44} and c_E modes. Here the mode $c_L = c_{44} + (c_{11} + c_{12})/2$ will be used. It is the longitudinal wave which propagates along the [110] axis. The isothermal modulus relating to the orthorhombic global minima of the APES is

$$(c_L^{JT})^T = -\frac{na_0^2}{k_B T}\left(\frac{4}{9}F_T^2 + \frac{1}{216}F_E^2\right) . \qquad (5.1)$$

One can see that this modulus depends upon both linear vibronic coupling constants. Thus, either after calculation of F_E^2 using α_E^{JT} (equation (3.36)) we can determine F_T^2, or after calculation of F_T^2 using α_T^{JT} (equation (3.37)) we can determine F_E^2. One more specificity of the attenuation dependences in CaF_2:Cr is the broad high-temperature shoulder of the relaxation peak. We can propose that it is determined by another contribution to attenuation. Seen in all the modes, it can be attributed to one or more JT subsystems with the triply degenerate orbital states which have larger relation rates and, therefore, possess larger values of T_1 (certainly, at the same frequency of the generated wave). For this reason, we will simulate the temperature dependence of attenuation with the use of three

mechanisms meaning that the agreement with the experimental curve can be expected only at low temperatures.

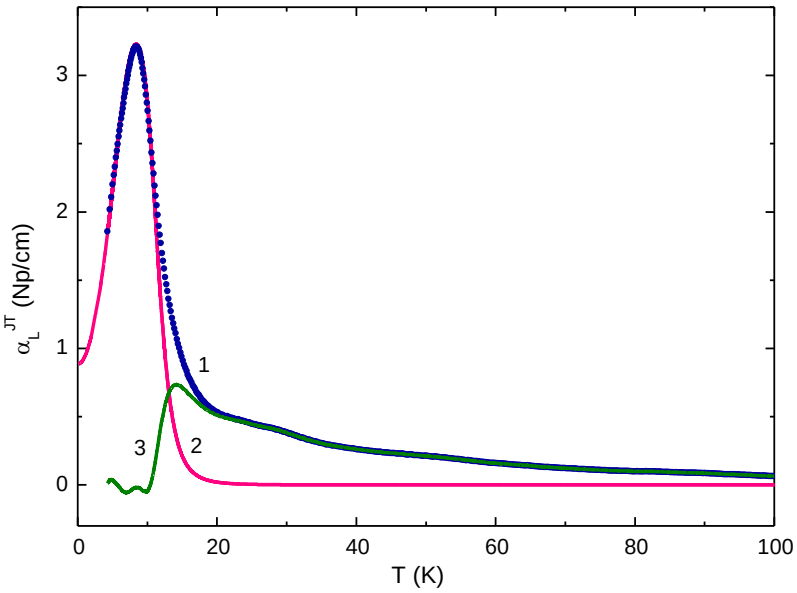

Figure 5.3 – Temperature dependence of the JT contribution to attenuation α_L^{JT} of the mode c_L measured at 54 MHz (curve 1 shown by the circles) and fitting curves α_L^m (curve 2) defined by equation (5.2) with $\alpha_L^{JT}(T_1)\cdot T_1 = 28.9\ \mathrm{K}\cdot\mathrm{Np}\cdot\mathrm{cm}^{-1}$ and relaxation time τ shown in Figure 5.4. See the magnitudes of fitting parameters in the text. Curve 3 is the difference $\Delta\alpha_L^{JT} = \alpha_L^{JT} - \alpha_L^m$ (in this case α_L^m is represented by the curve 2).

During attestation of the samples, no impurities were detected of a comparable with Cr concentration. Therefore, we can accept that the shoulder is formed by the subsystem of Cr^{3+} ions in cation lattice positions. Cr^{3+} ion has the ground orbital triplet $^4T_{1g}(t_{2g}e_g^2)$ in high spin configuration (see Table 1 in [33]). A nonlocal or local charge compensator is requires for aliovalent substitution. In the latter case, compensation is carried out by a fluorine vacancy near the impurity ion or by introducing an excess fluorine ion into the nearest interstitial position. The fluorine vacancies seem unlikely in the presence of fluorine in the crystal growth atmosphere. The anomaly caused by $Cr^{3+}F_8^-$ complexes overlaps with the region of activation relaxation of the $Cr^{2+}F_8^-$ sub-system. By analogy with Cr^{3+} in SrF_2 matrix

[80] we propose that in our crystal, every $Cr^{3+}F_8^-$ complex is distorted along one of the tetragonal axes due to F^- compensator located in the neighboring cubic cave. This distortion has electrostatic, non-JT nature but lead to elongation (contraction) of the edges and diagonals of the complexes. The expressions for the energy changes caused by the additional non-JT deformations were presented in chapter 3 (see equations (3.1)-(3.18)). As a result, instead of one well-resolved peak (which occurs when deformations of the complexes have only JT origin) a number of attenuation maxima can be formed in a certain temperature range. In a sense, this phenomenon is similar to off-center problem (see [81, 82] and references therein).

To determine the activation energy for the $Cr^{2+}F_8^-$ complexes, we have performed a simulation of contribution of the JT sub-system to ultrasonic attenuation with account of all three mechanisms of relaxation and have derived the magnitude of V_0 with the help of fitting procedure. The result of such fitting is shown in Figure 5.3. Contribution to attenuation of the c_L mode, α_L^{JT} (curve 1), was defined as the difference between the measured attenuation $\Delta\alpha_L(T)$ in CaF_2:Cr and in CaF_2 (presented by the curves 1 and 2 in Figure 5.2, respectively). The model dependence was taken in the form of

$$\alpha_\beta^{JT} = 2\frac{\alpha_\beta^{JT}(T_1)\cdot T_1}{T}\frac{\omega\tau}{1+(\omega\tau)^2}, \tag{5.2}$$

which follows from equation (1.21) with $\tau = \left(\tau_a^{-1}+\tau_t^{-1}+\tau_R^{-1}\right)^{-1}$ and $\beta = L$. The fitting parameters which characterize the mechanisms of relaxation are $\tau_0 = 3\cdot10^{-13}$ s, $V_0 = 132$ K, $B^{-1} = 1.9\cdot10^{-7}$ s·K, and $(B/\Theta^2)^{-1} = 3.1\cdot10^{-6}$ s·K^3.

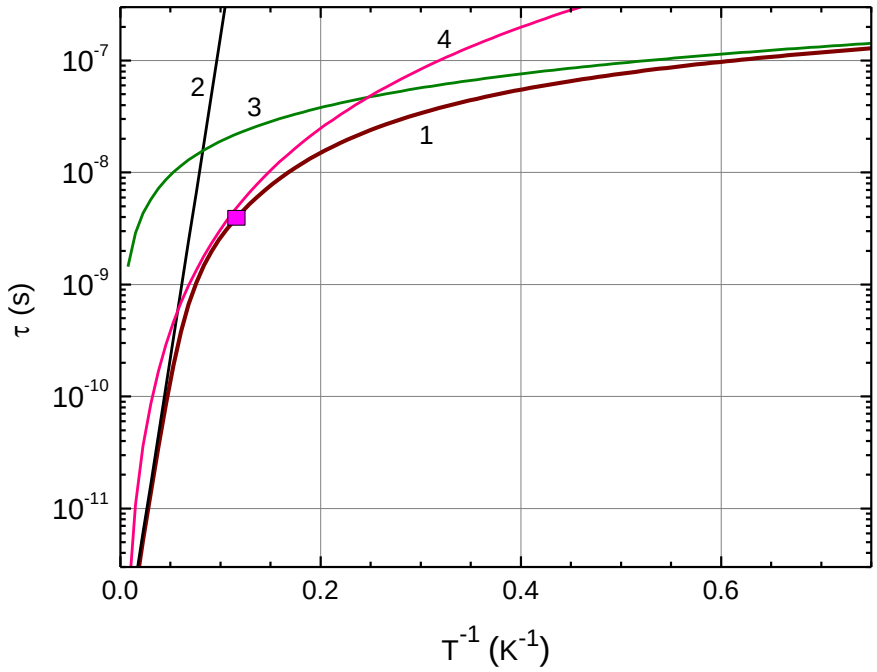

Figure 5.4 – Relaxation time as the result of $\alpha_L^{JT}(T)$ fitting presented in Figure 5.3. $\tau = \left(\tau_a^{-1} + \tau_t^{-1} + \tau_R^{-1}\right)^{-1}$, **).** Curve 1 represents $\tau = \left(\tau_a^{-1} + \tau_t^{-1} + \tau_R^{-1}\right)^{-1}$, curve 2 is $\tau_a = 3 \cdot 10^{-13} \exp(132/T)$, curve 3 is $\tau_t = 1.9 \cdot 10^{-7} T^{-1}$ and curve 4 is $\tau_R = 3.1 \cdot 10^{-6} \cdot T^{-3}$.

The result of fitting $\tau(1/T)$ is shown in Figure 5.5. Curve 6 represents simulation with account of only the tunneling mechanisms: one can see that this curve describes well the experimental dependence only below 9 K. Curve 2 calculated with account of all three mechanisms using $V_0 = 132$ K coincides with the experimental curve below 10.5 K. It is the most wide temperature interval among all the model curves. Thus, we can state that activation energy can be accepted as $V_0 = 132 \pm 7$ K.

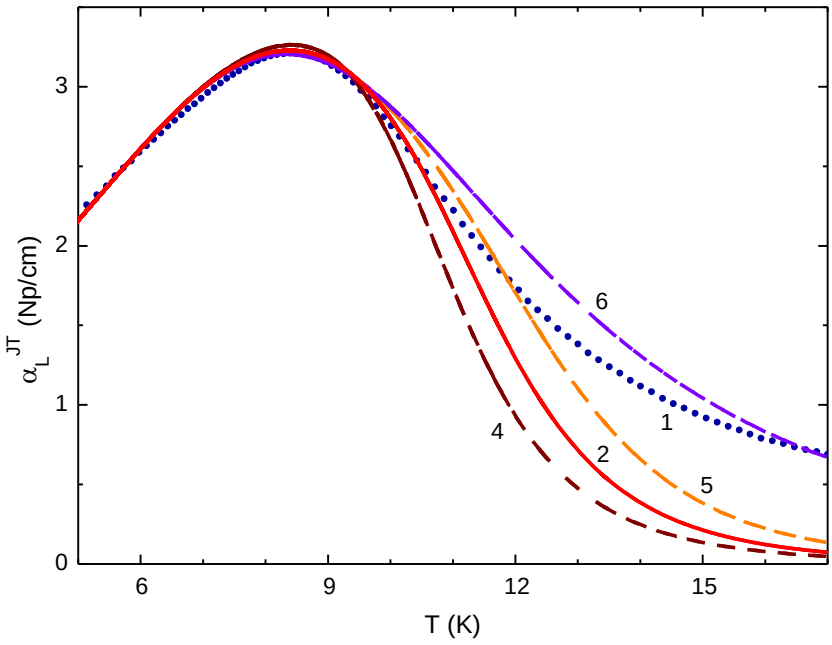

Figure 5.5 – Temperature dependence of the JT contribution to attenuation α_L^{JT} of the c_L mode measured at 54 MHz and fitting curves defined by equation (5.2) with $\alpha_L^{JT}(T_1)\cdot T_1 = 28.9\ \mathrm{K\cdot Np\cdot cm^{-1}}$. The curves (1 and 2) are the same as in Figure 5.2. Curves 4 and 5 are described as curve 2 but with $V_0 = 124$ K and 144 K, respectively. Curve 6 calculated without account of activation mechanism, e.g., $\tau = \left(\tau_t^{-1} + \tau_R^{-1}\right)^{-1}$.

5.3. Concentration of the $Cr^{2+}F_8^{-}$ complexes

The magnitude of concentration of the JT complexes is required for calculation of the linear vibronic coupling constants F_E [equation (3.36)] and F_T [equation (3.37)] or

$$F_T = \left[9\frac{c_0 k_B}{n a_0^2}\frac{\alpha_L^{JT}(T_1)\cdot T_1}{k_0} - \frac{F_E^2}{96}\right]^{1/2}, \qquad (5.3)$$

provided F_E is determined already. In the case of CaF_2:Cr the attestation procedure provides the total amount of the chromium ions $n = (4.74 \pm 0.03)\cdot 10^{19}\ \mathrm{cm^{-3}}$. We propose that our specimen contains only Cr^{2+} and Cr^{3+}. To estimate the content of Cr^{3+} ions we carried out a simulation of the high temperature contribution of the

$Cr^{3+}F_8^-$ subsystem to the longitudinal wave attenuation (denoted as $\Delta\alpha_L^{JT}$ and defined in caption of Figure 5.3) assuming that low-temperature contribution initiated by the tunneling mechanisms are negligible due to high-temperature position of the anomalies (with respect to ones caused by the $Cr^{2+}F_8^-$ subsystem). Simulation of the α_L^{JT} was done with the help of 4 summands defined as

$$\left[\alpha_L^{JT}(T)\right]_i = k_i 2\frac{\alpha_L^{JT}(T_1)\cdot T_1}{T}\frac{\omega\tau_i}{1+(\omega\tau_i)^2}, \tag{5.4}$$

where $i=1,2,3,4$, $\alpha_L^{JT}(T_1)\cdot T_1$ is the measured values relating to the low-temperature anomaly (caused by $Cr^{2+}F_8^-$ subsystem). Since the tunneling mechanisms are less effective at high temperatures in comparison with the thermal activation, we took into account only activation mechanism:

$$\tau_i = \tau_{0i}\exp(V_{0i}/T). \tag{5.5}$$

The parameters τ_{0i} and V_{0i} define the position of the peaks in *T*-scale, while the coefficients k_i determine their peak value, indicate the difference of a certain peak with respect to the anomaly caused by the Cr^{2+} centers and depend on the isothermal modulus as follows

$$k_i = \frac{\left[(c_L^{JT})^t\right]^{(3+)}}{\left[(c_L^{JT})^t\right]^{(2+)}} = \frac{n^{(3+)}}{n^{(2+)}}\frac{\left[(F_E{}^{3+})^2+96(F_T^{(3+)})^2\right]}{\left[(F_E{}^{2+})^2+96(F_T^{(2+)})^2\right]}. \tag{5.6}$$

The subscripts $(2+)$ or $(3+)$ indicate the chromium ion charge to which the parameter relates. The magnitudes of the peaks were chosen according to the requirement: the model attenuation curve being the sum of four contributions (curve 2 in Figure 5.6) should oscillate over curve 1 which is the difference between the attenuation caused by both $Cr^{2+}F_8^-$ 8 and $Cr^{3+}F_8^-$ sub-systems (curve 1 in Figure 5.3) and attenuation caused by the Cr^{2+} centers (curve 2 in Figure 5.3). We assumed that account of distribution of the static distortions (or oscillations of the interstitial fluorine ion in the cave) should make the model curve more smooth and

should approach it the curve 13 in Figure 5.3 (i.e., the square under the curve 2 should be constant).

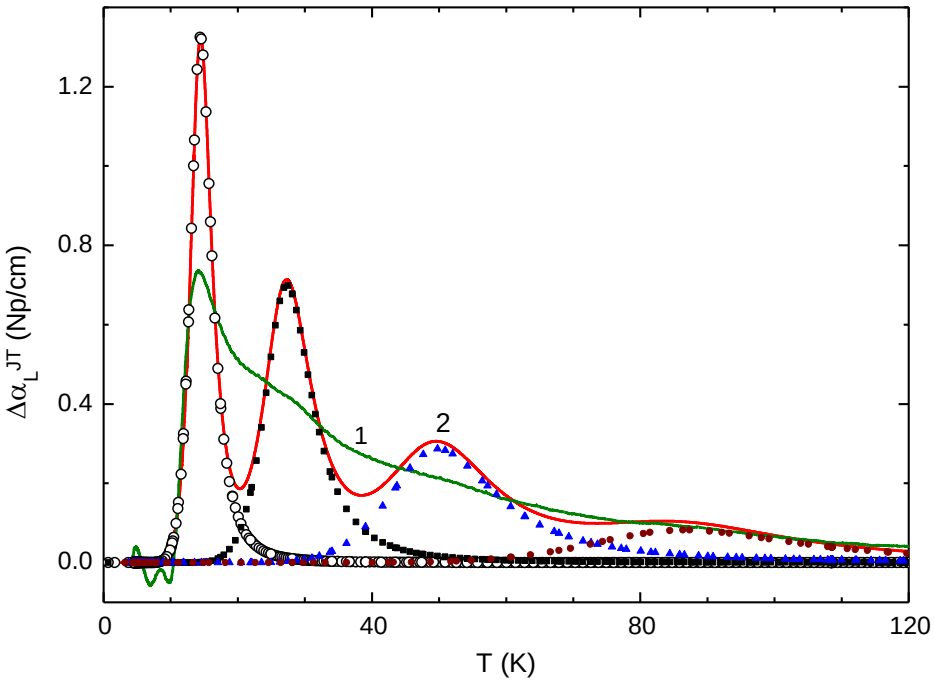

Figure 5.6 – Temperature dependence of $\Delta\alpha_L^{JT} = \alpha_L^{JT} - \alpha_L^m$ at $\omega/2\pi$ = 54MHz (curve 1, in Figure 5.3 it is curve 3) and model curve (2) which summands are given by the symbols and defined by equations (5.3)-(4.4) with $\alpha_L^{JT}(T_1)\cdot T_1 = 28.9\ \mathrm{K\cdot Np\cdot cm^{-1}}$. Open circles: $k_1 = 2/3$, $\tau_1 = 10^{-13}\exp(150/T)$; squares: $k_2 = 2/3$, $\tau_2 = 5\cdot10^{-13}\exp(240/T)$; triangles: $k_3 = 1/2$, $\tau_3 = 3\cdot10^{-12}\exp(350/T)$; filled circles : $k_4 = 1/4$, $\tau_4 = 6\cdot10^{-12}\exp(550/T)$.

If we propose that the vibronic coupling constants of Cr^{2+} and Cr^{3+} centers are equal, our model calculations points out the relation between the Cr^{2+} and Cr^{3+} concentrations $n^{(2+)}/n^{(3+)} \approx 1/2$ (where $n^{(3+)} = \sum_{i=1}^{4} n_i^{(3+)}$). However, we must take into account the following: shift of the relaxation peak to higher temperatures indicates reduction of relaxation rate. The latter evidences deeper global minima of the $Cr^{3+}F_8^-$ APES that can be only due to higher vibronic coupling constants. So, we assume that the vibronic coupling constants of the Cr^{3+} centers exceed ones of the Cr^{2+} centers by the factor of $\sqrt{2}$. As a result, we come to the conclusion about

approximate equal concentration of both the ions in the crystal. Thus, we used $n^{(2+)} = n/2$ in our further calculations.

We would like to emphasize an importance of such account of concentration of the JT centers. The high-temperature shoulder of the attenuation peak is not high and, at the first glance, could be caused by a subsystem of much lower concentration than $n^{(2+)}$. But (i) it is broad enough, so its integral contribution is not small; (ii) the shoulder is observed at higher temperatures that (iii) compels us to assume higher magnitude of the vibronic constants of the $Cr^{3+}F_8^-$ complexes and (iv) results in reduction of its contribution by the factor $1/T$ [see equation (5.4)]. Therefore, the visually small anomaly proved to be caused by the subsystem of a comparable concentration of the JT centers. Neglecting the $Cr^{3+}F_8^-$ subsystem and assuming $n^{(2+)} = n$ would lead to underestimating the vibronic coupling constants by the factor of $\sqrt{2}$ [see equations (3.36), (3.37), (5.3)] and the JT stabilization [see equations (3.34) and (3.35)] by the factor of 2.

5.4. Parameters of the adiabatic potential energy surface

Now we can reproduce once more the procedure described by equations (3.34)-(3.45) with the following magnitudes of the entering constants: $\omega_R = 145\ \text{cm}^{-1}$ [79], $c_{11} = 17.4 \cdot 10^{11}\ \text{dyn/cm}^2$, $c_{12} = 5.6 \cdot 10^{11}\ \text{dyn/cm}^2$, $c_{44} = 3.593 \cdot 10^{11}\ \text{dyn/cm}^2$ measured at $T = 4.2\ \text{K}$ [83]. The linear vibronic coupling constants and the JT stabilization energies calculated with $M = (m_{Cr} : 8m_F) / (m_{Cr} + 8m_F) = 6.43 \cdot 10^{-23} g$, $K_T = 4.84 \cdot 10^4\ \text{dyn/cm}$, $K_E = 8.14 \cdot 10^4\ \text{dyn/cm}$, and $a_0 = 2.36\ \text{Å}$ [79]. As a result, we obtain the magnitudes of the vibronic coupling constants and the APES parameters presented in Tables 5.1 and 5.2. We believe that the main contribution to the error caused by the measurement procedure contributes $\Delta\alpha_\beta(T)$ (see paragraph 2.2). However, even more uncertainty is introduced by the concentration of Cr^{2+} ions, $n^{(2+)}$. Therefore, the magnitudes given in Tables 5.1-5.2 should be accepted as estimates.

Table 5.1 – Stabilization energies for tetragonal, trigonal and orthorhombic APES extrema.

E_E, cm^{-1}	E_T, cm^{-1}	E_{OR}, cm^{-1}
208	538	697

Table 5.2 – Vibronic coupling constants and parameters $Q_{0\vartheta}^{OR}$, $Q_{0\zeta}^{OR}$, Q_0^E and Q_0^T entering Tables 3.2–3.4. Two magnitudes of W_{ET}, $Q_{0\vartheta}^{OR}$, $Q_{0\zeta}^{OR}$ for one set of (F_E, F_T) originate from two solutions of the quadratic equation (3.44) with respect to A.

F_E, dyn	F_T, dyn	W_{ET}, dyn/cm	Q_0^E, Å	Q_0^T, Å	$Q_{0\vartheta}^{OR}$, Å	$Q_{0\zeta}^{OR}$, Å
$8.2\cdot10^{-5}$	$8.8\cdot10^{-5}$	$-2.6\cdot10^{4}$	0.10	0.12	-0.13	0.25
		$5.2\cdot10^{4}$			0.22	0.42
$-8.2\cdot10^{-5}$	$-8.8\cdot10^{-5}$	$-2.6\cdot10^{4}$	-0.10	-0.12	0.13	-0.25
		$5.2\cdot10^{4}$			-0.22	-0.42
$8.2\cdot10^{-5}$	$-8.8\cdot10^{-5}$	$-2.6\cdot10^{4}$	0.10	-0.12	-0.13	-0.42
		$5.2\cdot10^{4}$			0.22	-0.25
$-8.2\cdot10^{-5}$	$8.8\cdot10^{-5}$	$-2.6\cdot10^{4}$	-0.10	0.12	0.13	0.25
		$5.2\cdot10^{4}$			-0.22	0.42

5.5. Conclusion

1. In $CaF_2:Cr^{2+}$ single crystal, manifestation of the JTE proved to be similar to one in $SrF_2:Cr^{2+}$ and $CaF_2:Ni^{2+}$, although the JT ions or host crystals are different.

2. In all the crystals, APES obeys orthorhombic global minima and subject to the quadratic $T \otimes (e + t_2)$ JTE problem.

3. The relaxation attenuation peak was observed at relatively low temperatures (approximately 8.7 K at about 54 MHz) in $CaF_2:Cr^{2+}$. Lower temperature of the peak location means higher relaxation rate and lower potential energy barrier (or activation energy).

4. The potential energy barrier increased with increase of ionic radius of the dopant ($Cr^{2+} \rightarrow Ni^{2+}$) and with increase of ionic radius of the matrix cation ($Ca^{2+} \rightarrow Sr^{2+}$). In this context, another 3*d* ion in CaF_2 crystal is interesting to investigate.

CHAPTER 6. ADIABATIC POTENTIAL ENERGY SURFACE OF THE JAHN-TELLER COMPLEXES IN $CaF_2:Cu^{2+}$ CRYSRAL

6.1. Temperature dependences of dynamic elastic moduli

In this chapter, we will show how the procedures of the APES parameters determination can be performed with the use of the experimental data on both dissipation and dispersion. The procedures will be realized which are based on the data on temperature dependence of attenuation and on the data on temperature dependence phase velocity. These two approaches represent the results of quite different independent experiments. They can serve as verification of the validity of both the methods. For more convenient presentation of the experimental data we will discuss the properties of the JT subsystem in terms of real and imaginary parts of the dynamic (i.e., frequency dependent) elastic moduli. Equation (1.21) shows how parts of a modulus relate to the phase velocity and attenuation of a wave.

Figures 6.1 and 6.2 show the temperature dependences the longitudinal $c_L = c_{44} + (c_{11} + c_{12})/2$ and tetragonal $c_E = (c_{11} - c_{12})/2$ moduli in CaF_2:Cu^{2+}. These moduli are associated with the normal modes which propagate along the 110 crystallographic axis, polarization of the shear mode is along the $[1\bar{1}0]$ axis. One can see the typical for the JTE manifestation anomaly of relaxation nature. Relaxation-nature anomalies were observed in the c_{44} mode also. Therefore, we can conclude that the $Cu^{2+}F_8$ JT complex possesses the orthorhombic global minima of the APES and subject to quadratic $T \otimes (e + t_2)$ JTE problem, like all the other complexes studied in our dissertation.

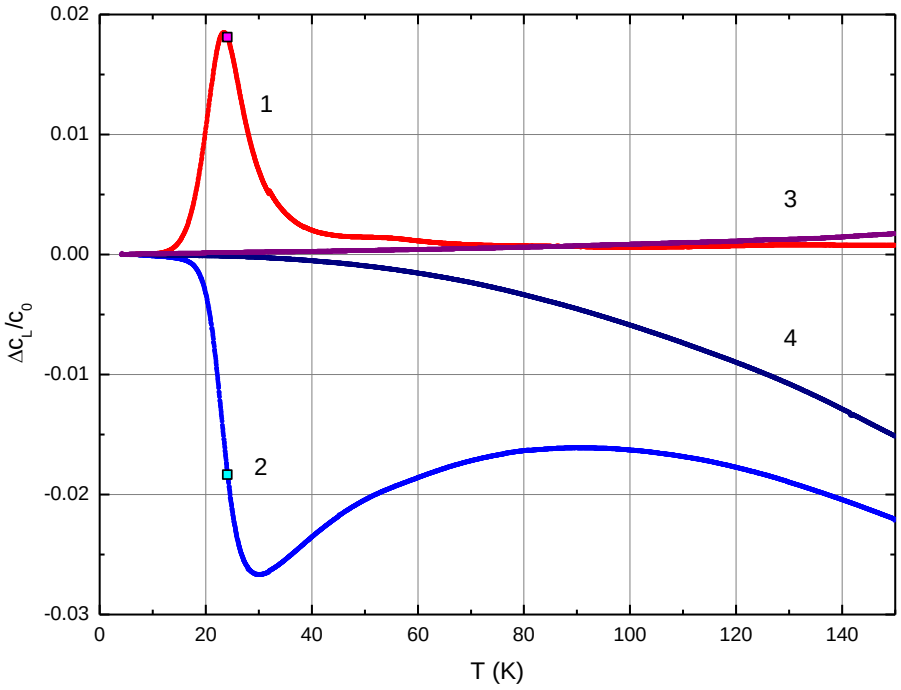

Figure 6.1 – Temperature dependences of the imaginary (curve 1) and real (2) parts of the elastic modulus $c_L = c_{44} + (c_{11} + c_{12})/2$ measured at 55.8 MHz in CaF_2:Cu^{2+} crystal. The same dependences but measured 55.5 MHz in nominally pure CaF_2 are shown by the curves 3 and 4. $\Delta c_L = c_L(T) - c_0$, $c_0 = c_L(T_0)$, $T_0 = 4.2$ K. The squares correspond to $\omega\tau = 1$.

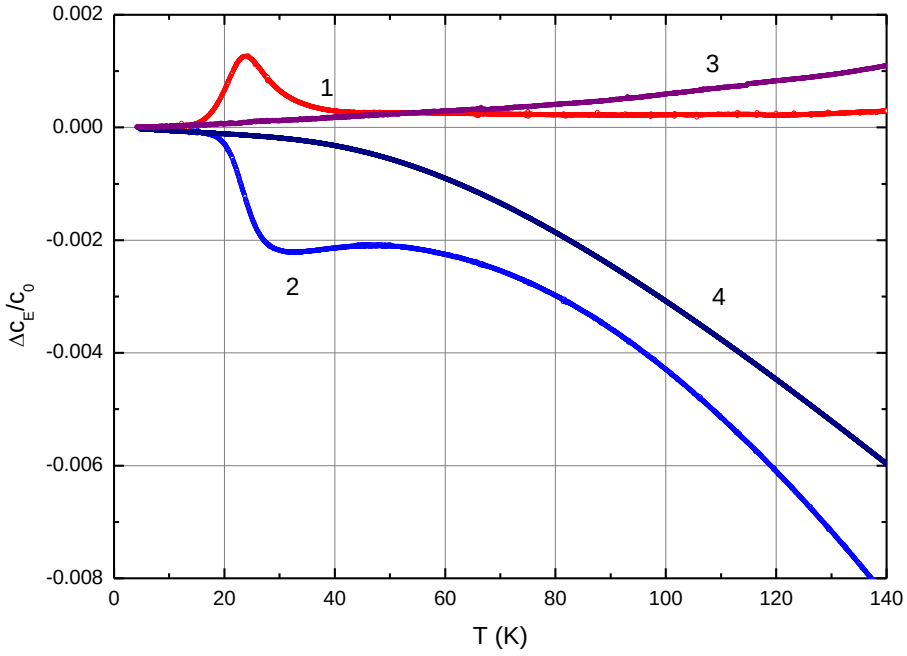

Figure 6.2 – Temperature dependences of the imaginary (curve 1) and real (2) parts of the elastic modulus $c_E = (c_{11} - c_{12})/2$ measured at 59.6 MHz in CaF_2:Cu^{2+} crystal. The same dependences but measured 57.1 MHz in nominally pure CaF_2 are shown by the curves 3 and 4. $\Delta c_E = c_E(T) - c_0$, $c_0 = c_E(T_0)$, $T_0 = 4.2$ K.

6.2. JT contribution to the elastic moduli

The contribution of the JT subsystem to the elastic moduli manifests itself as a peak in the imaginary part and a minimum in the real part in the vicinity of T_1 as it can be seen in Figures 6.1 and 6.2. Remind, the temperature T_1 is determined from the condition $\omega \cdot \tau(T_1) = 1$. As follows from Table 1, the isothermal elastic moduli are inversely proportional to the temperature. Therefore, the position of the peak in $\mathrm{Im}\,\Delta c_\beta(T)/c_0$, in fact, does not coincide with T_1. However, the value of T_1 can be determined from the maximum of the function $\left[\mathrm{Im}\,\Delta c_\beta(T)/c_0\right]\cdot T$ like it was done in section 3.2 respectively $\left[\Delta\alpha_{44}^{JT}(T)\right]\cdot T$ (see also Figure 3.3). To use this approach we must define the JT contribution to the elastic moduli. Taking into account the T_1 definition, the equation (1.21) can be transformed into

$$\frac{c_\beta^{JT}}{c_0} = 2\frac{\mathrm{Re}\left[c_\beta^{JT}(T_1)\right]}{c_0}\frac{T_1}{T}\frac{1}{1+(\omega\tau)^2} + 2i\frac{\mathrm{Im}\left[c_\beta^{JT}(T_1)\right]}{c_0}\frac{T_1}{T}\frac{\omega\tau}{1+(\omega\tau)^2}, \qquad (6.1)$$

Moreover, it follows from the equation (1.21) that

$$\mathrm{Re}\left[c_\beta^{JT}(T_1)\right] = -\mathrm{Im}\left[c_\beta^{JT}(T_1)\right], \qquad (6.2)$$

The JT anomalies in CaF_2:Cu^{2+} are observed at lower temperatures in comparison with ones in CaF_2:Ni^{2+}. Lower potential energy barriers can be expected in this case, higher level of the low temperature attenuation and, therefore, we must apply the approach described in chapter 5, i.e., simulation of the temperature dependence of $\left[\mathrm{Im}\,\Delta c_\beta(T)/c_0\right]$ with account of the temperature dependence of the background contribution to $\Delta c_\beta(T)$ and simulation of the dependence with the use of three mechanism of relaxation given by the equations (3.28) - (3.30). So, (i) the background contributions (which are the temperature dependences of the moduli of the CaF_2 crystal) should be extracted from the measured $\Delta c_\beta(T)/c_0$ in CaF_2:Cu^{2+} and (ii) the low-temperature limit of $\mathrm{Im}\left[c_\beta(T)/c_0\right]$ should be added to $\mathrm{Im}\,\Delta c_\beta(T)/c_0$ since the variation of the modulus but not the modulus itself is measured in an experiment. In the process of simulation, the following fitting parameters were used: $\mathrm{Re}\left[c_\beta^{JT}(T_1)\right]\cdot T_1/c_0$, $\mathrm{Im}\left[c_\beta^{JT}(T_1)\right]\cdot T_1/c_0$, τ_0 , V_0 , B , B/Θ^2 . The first two fitting parameters define the scale of variation of c_β^{JT} (its real and imaginary parts) and must correspond to equation (6.2). The remaining ones specify the functional dependence of relaxation time

$$\tau = \left(\tau_a^{-1} + \tau_t^{-1} + \tau_R^{-1}\right)^{-1} . \qquad (6.3)$$

The experimental data (presented in Figure 6.2) multiplied by T are shown in Figure 6.3 (curves 1 and 2). Both the model curves 3 and 4 are calculated with the same relaxation time $\tau(T)$. The experimental and model curves coincide at the temperature below 30 K. They diverge at higher temperatures. There are some

reasons for such discrepancy. The expression for the relaxation time written by taking into account the three mechanisms corresponds to low temperatures, when the JT complexes are at the lowest energy levels at the APES minima. As the temperature rises, higher-energy levels [which are ignored in equations (3.1)-(3.18)] begin to be populated, and there will be no longer such simple expressions for both the relaxation time and the isothermal elastic moduli.

$\mathrm{Re}\left[c_L^{JT}(T_1)\right]\cdot T_1/c_0$ and $\mathrm{Im}\left[c_L^{JT}(T_1)\right]\cdot T_1/c_0$ slightly differ in absolute value, though they must be equal. This difference can be explained by the fact that the temperature dependence of the background attenuation (corresponding to a nominally pure crystal) is weak, especially at low temperatures, while the relaxation attenuation is much larger. Therefore, the error in determining the background attenuation affects insignificantly the result. In contrast, the real parts of the elastic moduli referring to the impurity and pure crystals have temperature changes comparable in magnitude, which, naturally leads to a larger error.

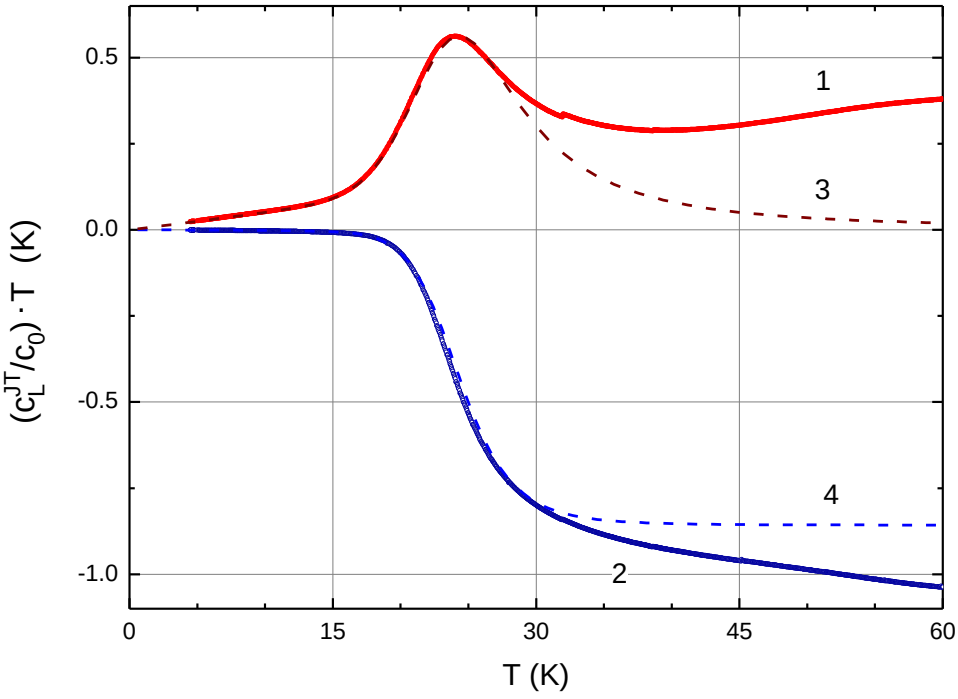

Figure 6.3 – Temperature dependences of the imaginary (curve 1) and real (2) parts of $\left[c_L^{JT}(T)\right]\cdot T\ /c_0$ (curve 1) and real (curve 2) parts of $c_L^{JT}(T)\cdot T/c_0=\left[\Delta c_L(T)-\Delta c_L^b(T)+i\,\mathrm{Im}\,c_L^{JT}(T\to 0)\right]\cdot T/c_0$, where $\Delta c_L^b(T)/c_0$ relates to the elastic modulus of the nominally pure crystal. Curves 3 and 4 represent the model curves obtained at $\mathrm{Re}\left[c_L^{JT}(T_1)\right]\cdot T_1/c_0=-0.429$ K, $\mathrm{Im}\left[c_L^{JT}(T_1)\right]\cdot T_1/c_0=-0.562$ K, $\tau_a=3\cdot 10^{-12}\exp(170/T)$ s , $\tau_t=6.5\cdot 10^{-7}/T$ s , $\tau_R=2\cdot 10^{-3}/T^3$ s.

Using fitting, which results are presented in Figure 6.3, we determine all of the parameters that characterize the relaxation time. The activation energy V_0 , which specifies the potential barrier between the APES minima, is the most significant of them. Therefore, it is important to make sure that our modeling is reliable, inspite of the large number of fitting parameters. Having determined the low-temperature JT contribution to the elastic moduli using only two parameters for this purpose, $\mathrm{Im}\left[c_L^{JT}(T_1)\right]\cdot T_1/c_0$ and B (or, more precisely, their product, i.e., actually one parameter), we can construct the temperature dependence of the relaxation time and determine V_0 from it.

Note that the temperature dependence of the relaxation time can also be derived from the data on $\mathrm{Re}\left[c_\beta^{JT}(T)\right]/c_0$ by measuring the ultrasound velocity $\Delta v_\beta(T)/v_0$ in the doped and nominally pure crystals. They have comparable temperature changes, which affects the accuracy of determining $\mathrm{Re}\left[c_\beta^{JT}(T)\right]\cdot T/c_0$ and, hence, $\tau(T)$.

The optimal variant is to construct the temperature dependence of the relaxation time both from the data on attenuation and from the data on dispersion. These are completely independent measurements. Moreover, the results are processed using different formulas, which give a good tool for verifying the obtained results.

6.3. Temperature dependence of relaxation time

The starting point for derivation the expressions for the relaxation time basing on the data on c_β^{JT}/c_0 is equation (6.1) which can be presented in the form of

$$\mathrm{Re}\frac{c_\beta^{JT}(T)}{c_0}=2\frac{\mathrm{Re}\left[c_\beta^{JT}(T_1)\right]}{c_0}\frac{T_1}{T}\frac{1}{1+(\omega\tau)^2}, \tag{6.4}$$

$$\mathrm{Im}\frac{c_\beta^{JT}(T)}{c_0}=2i\frac{\mathrm{Im}\left[c_\beta^{JT}(T_1)\right]}{c_0}\frac{T_1}{T}\frac{\omega\tau}{1+(\omega\tau)^2}, \tag{6.5}$$

These equations can be solved with respect to τ :

$$\tau(T)=\frac{1}{\omega}\left\{\frac{\mathrm{Im}\,c_\beta^{JT}(T_1)\cdot(T_1)}{\mathrm{Im}\,c_\beta^{JT}(T)\cdot(T)}\pm\sqrt{\left[\frac{\mathrm{Im}\,c_\beta^{JT}(T_1)\cdot(T_1)}{\mathrm{Im}\,c_\beta^{JT}(T)\cdot(T)}\right]^2-1}\right\}, \tag{6.6}$$

$$\tau(T)=\frac{1}{\omega}\left\{\sqrt{\frac{\mathrm{Re}\,c_\beta^{JT}(T_1)\cdot(T_1)}{\mathrm{Re}\,c_\beta^{JT}(T)\cdot(T)}-1}\right\}. \tag{6.7}$$

The dependences $\tau(T)$ calculated with the use of equations (6.6) and (6.7) written for $\beta=L$ are shown in Figure 6.4. It can be seen that both the dependences almost coincide at temperatures below 25 K. Differences arise at higher temperatures, and

the causes of these differences are the same as those in the case of a difference between the experimental dependences of the components of the elastic moduli and the model curves that take into account only the energy of the ground states at the APES minima and the transition processes between them (shown in Figure 6.3).

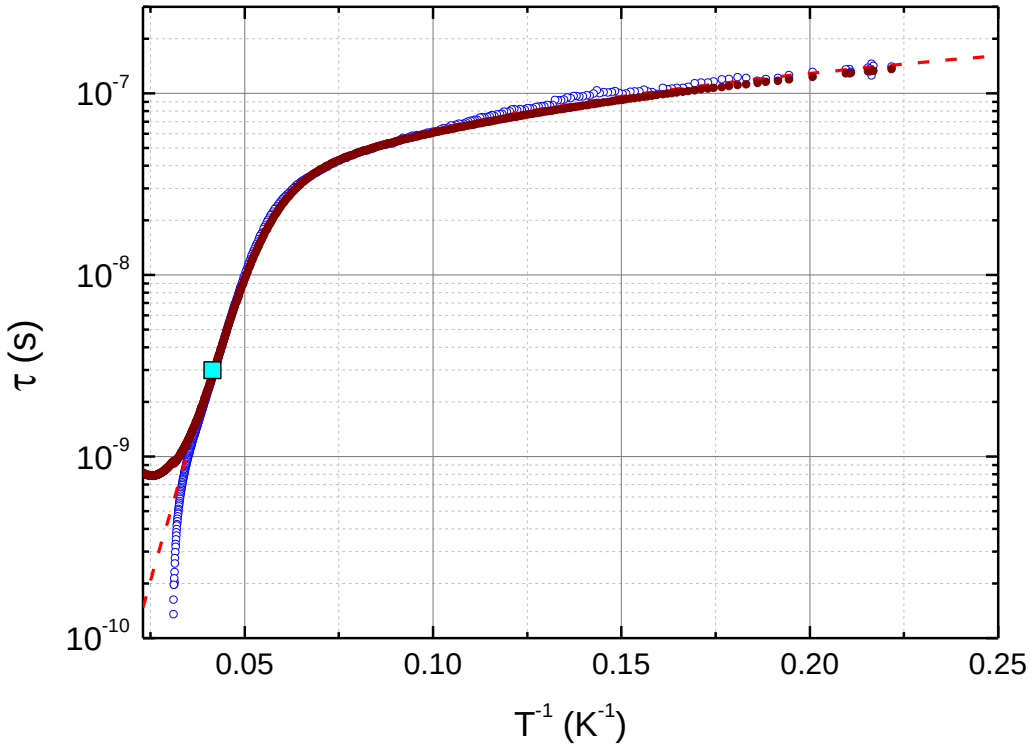

Figure 6.4 – The relaxation time versus inverse temperature, based on $\mathrm{Re}\left[c_L^{JT}(T)\right]/c_0$ (brown symbols) and $\mathrm{Im}\left[c_L^{JT}(T)\right]/c_0$ (blue open circles) at 55.8 MHz . The dashed curve indicates the result of modeling the relaxation time $\tau=\left(\tau_a^{-1}+\tau_t^{-1}+\tau_R^{-1}\right)^{-1}$ taking into account the three mechanisms characterized by the relaxation times τ_a , τ_t, and τ_R which values are given in the caption to Figure 6.3. The square symbol corresponds to the condition $\omega\tau=1$.

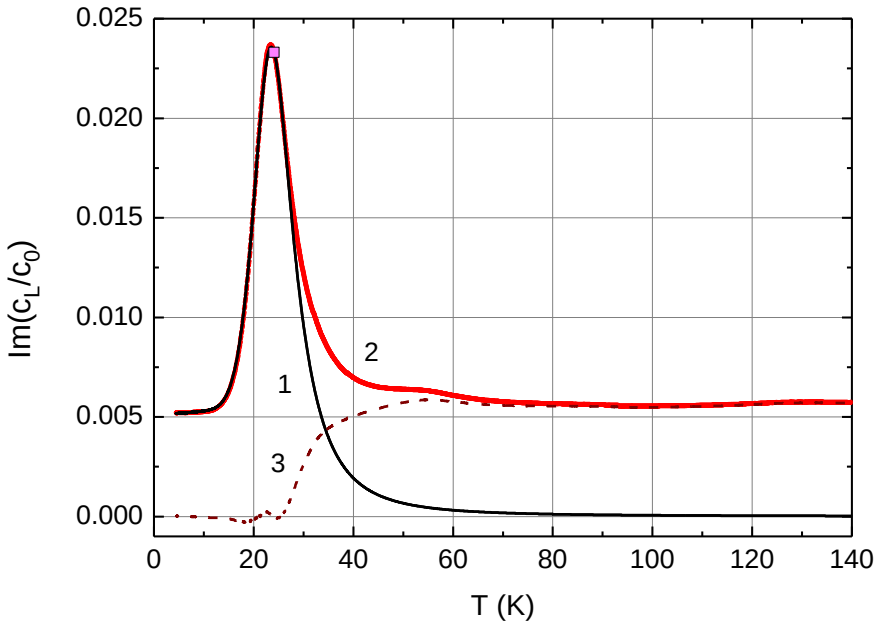

Figure 6.5 – Temperature dependences of the JT contribution to the $\mathrm{Im}\left[c_L^{JT}(T)\right]/c_0$: curve 1 is model calculation with the use of equation (6.5) and the entering values $\mathrm{Im}\left[c_L^{JT}(T_1)\right]\cdot T_1/c_0 = -0.562$ K, $\tau_a = 3\cdot 10^{-12}\exp(170/T)$ s, $\tau_t = 6.5\cdot 10^{-7}/T$ s, $\tau_R = 2\cdot 10^{-3}/T^3$ s, $\omega/2\pi = 55.8$ MHz; curve 2 is the experimental curve $\mathrm{Im}\left[c_L(T)\right]/c_0$; dashed curve 3 is the difference between these dependences. The square symbol corresponds to the condition $\omega\tau = 1$.

To make sure that the parameters describing the low-temperature relaxation were chosen correctly, Figure 6.5 presents the model curve $\mathrm{Im}\left[\,c_L^{JT}(T)\right]_{mod}/c_0$ (curve 1) calculated using equation (6.5) and the values for $\mathrm{Im}\left[c_L^{JT}(T_1)\right]\cdot T_1/c_0$ and the expressions for τ_a, τ_t, and τ_R given in the captions to Figure 6.3, curve 2 is $\mathrm{Im}\left[c_L(T)\right]/c_0$, i.e., the temperature dependence of the JT contribution to the imaginary component of the longitudinal elastic modulus, which is the experimental dependence $\mathrm{Im}\left[\Delta c_L(T)\right]/c_0$ shifted by $\mathrm{Im}\left[\,c_L^{JT}(T\to 0)\right]_{mod}/c_0$, and the dashed curve 3 is the difference between these dependences. It can be seen that at temperatures below 25 K the difference between the experimental and model curves is minimal,

suggesting that the assertion about the three relaxation mechanisms at low temperatures is valid and that the choice of the parameters characterizing these mechanisms is correct.

6.4. Parameters of the adiabatic potential energy surface

Equations (3.36), (3.37), and (5.3) rewritten for $\mathrm{Im}\left[\, c_\beta^{JT}(T)\right]$ discussed in this chapter instead $\alpha_\beta^{JT}(T)$ have the following form

$$F_E^2 = 144\frac{c_{E0}k_B}{na_0^2}\frac{\mathrm{Im}\left[c_E^{JT}(T_1)\right]\cdot T_1}{c_{E0}}, \tag{6.7}$$

$$F_T^2 = \frac{9}{2}\frac{c_{T0}k_B}{na_0^2}\frac{\mathrm{Im}\left[c_T^{JT}(T_1)\right]\cdot T_1}{c_{T0}}, \tag{6.8}$$

$$F_T^2 = \frac{9}{2}\frac{c_{L0}k_B}{na_0^2}\frac{\mathrm{Im}\left[c_L^{JT}(T_1)\right]\cdot T_1}{c_{L0}} - \frac{F_E^2}{96}, \tag{6.9}$$

where $c_{\beta 0} = c_\beta(T_0)$, $\beta = E,T,L$. The JT stabilization energies corresponding to tetragonal E^E and trigonal E^T saddle points are determined using equations (3.34) and (3.35). It is assumed that the primary force constants can be specified as $K_T = M\omega_R^2$ with the reduced mass $M = (m_{Cu}:8m_F)\ /\ (m_{Cu}+8m_F)$, radial vibronic frequency $\omega_R = \omega_\tau = 145\ \mathrm{cm}^{-1}$ [79], and K_E calculated with the use of equation (3.39). $c_{11} = 17.4\cdot 10^{11}\ \mathrm{dyn/cm}^2$, $c_{12} = 5.6\cdot 10^{11}\ \mathrm{dyn/cm}^2$, $c_{44} = 3.593\cdot 10^{11}\ \mathrm{dyn/cm}^2$ measured at $T = 4.2\ \mathrm{K}$ [83]. The linear vibronic coupling constants were calculated with $a_0 = 2.36\ \mathrm{\AA}$ [79] and the JT stabilization energies E^E and E^T with $K_E = 6.12\cdot 10^4\ \mathrm{dyn/cm}$ and $K_T = 3.64\cdot 10^4\ \mathrm{dyn/cm}$. Reproducing the procedure described by equations (3.34)-(3.45), we obtain the magnitudes of the vibronic coupling constants and the APES parameters presented in Tables 6.1 and 6.2.

Table 6.1 – Stabilization energies for tetragonal trigonal and orthorhombic APES extrema.

E_E, cm^{-1}	E_T, cm^{-1}	E_{OR}, cm^{-1}
479	$1.11 \cdot 10^3$	$1.30 \cdot 10^3$

Table 6.2 – Vibronic coupling constants and parameters $Q_{0\vartheta}^{OR}$, $Q_{0\zeta}^{OR}$, Q_0^E and Q_0^T entering Tables 3.2–3.4. Two magnitudes of W_{ET}, $Q_{0\vartheta}^{OR}$, $Q_{0\zeta}^{OR}$ for one set of (F_E, F_T) originate from two solutions of the quadratic equation (3.44) with respect to A.

F_E, dyn	F_T, dyn	W_{ET}, dyn/cm	Q_0^E, Å	Q_0^T, Å	$Q_{0\vartheta}^{OR}$, Å	$Q_{0\zeta}^{OR}$, Å
$1.08 \cdot 10^{-4}$	$1.10 \cdot 10^{-4}$	$-1.55 \cdot 10^4$	0.176	0.201	-0.184	0.380
		$3.38 \cdot 10^4$			0.300	0.61
$-1.08 \cdot 10^{-4}$	$-1.10 \cdot 10^{-4}$	$-1.55 \cdot 10^4$	-0.176	-0.201	0.184	-0.380
		$3.85 \cdot 10^4$			-0.300	-0.618
$1.08 \cdot 10^{-4}$	$-1.10 \cdot 10^{-4}$	$-3.85 \cdot 10^4$	0.176	-0.201	0.300	-0.618
		$1.55 \cdot 10^4$			-0.184	-0.380
$-1.08 \cdot 10^{-4}$	$1.10 \cdot 10^{-4}$	$-3.85 \cdot 10^4$	-0.176	0.201	-0.300	0.618
		$1.55 \cdot 10^4$			0.184	0.380

6.5. Conclusion

1. In $CaF_2:Cu^{2+}$ single crystal, manifestation of the JTE proved to represent an intermediate case between $CaF_2:Cr^{2+}$ on one hand and $SrF_2:Cr^{2+}$ with $CaF_2:Ni^2$ on another hand, meaning that the relaxation anomalies are observed at approximately

24 K (at about 56 MHz) in comparison with $CaF_2:Cr^{2+}$ (8.7 K) $SrF_2:Cr^{2+}$ (56 K) and $CaF_2:Ni^{2+}$ (44 K).

2. In all the studied crystals, APES obeys orthorhombic global minima and subject to the quadratic $T \otimes (e + t_2)$ JTE problem.

3. Comparison of most of the parameters which characterize the JT complex is sophisticated by their some indeterminacy that is initiated by the uncertainty in determination of the concentration value. The method used in our research defines the total concentration of the impurity ions regardless their charge state. Whereas the expressions for calculation of the vibronic coupling constants and the JT stabilization energies contain concentration of definite ions. One more source of the error is inhomogeneity of the dopand distribution over the crystal. These two factors reduce the possible accuracy of the JTE parameters evaluation and further comparison of different complexes in various matrices.

4. Some parameters can be found which are not depend upon concentration. They are relaxation time and the ratio of the linear vibronic coupling constants. The first one is determined from the shape of the attenuation or dispersion curves but not on the scale of their variation. The second parameter is concentration independent since both the coupling constants have linear dependence on concentration of the JT complexes and their ratio does not depend on it.

5. Table 6.3 give an opportunity to compare V_0 and $|F_T / F_E|$ derived in our study. Besides, the modulus of F_T is also present in the table keeping in mind that the accuracy of its determination can be lower than of V_0 and of $|F_T / F_E|$.

6. Analyzing the data given in the Table 6.3, one can conclude: (i) the linear vibronic coupling constants characterizing the JT centers are approximately equal if to speak about their absolute values; (ii) activation energy characterizing the studied crystals is in the range of 90-400 cm^{-1} ; (iii) the order of the absolute value of the linear vibronic coupling constants F_E and F_T is 10^{-4} dyn.

Table 6.3. Activation energies and the linear vibronic constants of the JT complexes in the studied crystals

Crystal	Configu-ration	Ground state	V_0 , cm^{-1}	$\lvert F_T / F_E \rvert$	$\lvert F_T \rvert$, dyn
CaF_2:Cr^{2+} [A2]	d^4	${}^5T_{2g}\left(e_g^2 t_{2g}^2\right)$	91.7	1.07	$0.88 \cdot 10^{-4}$
CaF_2:Cu^{2+} [A3]	d^9	${}^2T_{2g}\left(e_g^4 t_{2g}^5\right)$	118	1.02	$1.1 \cdot 10^{-4}$
SrF_2:Cr^{2+} [A5]	d^4	${}^5T_{2g}\left(e_g^2 t_{2g}^2\right)$	264	1.04	$0.55 \cdot 10^{-4}$
CaF_2:Ni^2 [A1]	d^8	${}^3T_{1g}\left(e_g^4 t_{2g}^4\right)$	394	1.07	$1.2 \cdot 10^{-4}$

CONCLUSION

We have investigated the crystals with the fluorite structure with cation substitution by 3d ions: $CaF_2:Cr^{2+}$, $CaF_2:Cu^{2+}$, $CaF_2:Cu^{2+}$, and $CaF_2:Ni^{2+}$ with the use of ultrasonic technique. Temperature dependences of attenuation and phase velocity were measured in the range of 4-170 K. Relaxation anomalies caused by the subsystem of the cubic JT complexes $3d^{2+}F_8$ were observed in all the studied normal modes revealing the quadratic $T \otimes (e + t_2)$ JTE problem and the APES with the orthorhombic global minima.

We have considered a cubic JT complex with additional static non-JT deformations and have derived the expressions for its energy shifts caused by them. On the basis of the analysis of the obtained experimental data, we came to the conclusion that the additional static deformations are negligible for the isovalent substitution in our crystals.

The temperature dependence of relaxation time was obtained and simulated with account of three mechanisms. The simulation pointed out the more accurate value of the activation energy with respect to the data published earlier.

Manifestation of the JTE in $CaF_2:Ni^{2+}$ single crystal proved to be similar to one in $SrF_2:Cr^{2+}$, although the JT ions and host crystals are different. In both the crystals, the relaxation anomalies were observed at relatively high temperatures (approximately 56 and 44 K at about 55 MHz, respectively). Higher temperature of the peak location means lower relaxation rate and higher potential energy barrier (or activation energy provided that the vibronic frequency is the same). Comparison of the activation energies (570 and 380 K, respectively) supports this statement. The $Ni^{2+}F_8^-$ complexes in CaF_2 have larger magnitudes of the vibronic coupling constants and deeper extrema of the APES than $Cr^{2+}F_8^-$ complexes in SrF_2 matrix.

In $CaF_2:Cr^{2+}$ single crystal, the relaxation attenuation peak was observed at relatively low temperatures (approximately 8.7 K at about 54 MHz). Lower

temperature of the peak location means higher relaxation rate and lower potential energy barrier (or activation energy).

In $CaF_2:Cu^{2+}$ single crystal, manifestation of the JTE proved to represent an intermediate case between $CaF_2:Cr^{2+}$ on one hand and $SrF_2:Cr^{2+}$ with $CaF_2:Ni^2$ on another hand, meaning that the relaxation anomalies are observed at approximately 24 K (at about 56 MHz) in comparison with $CaF_2:Cr^{2+}$ (8.7 K) $SrF_2:Cr^{2+}$ (56 K) and $CaF_2:Ni^{2+}$ (44 K).

Comparison of most of the parameters which characterize the JT complex is sophisticated by their some indeterminacy that is initiated by the uncertainty in determination of the concentration value. The method used in our research defines the total concentration of the impurity ions regardless their charge state. Whereas the expressions for calculation of the vibronic coupling constants and the JT stabilization energies contain concentration of definite ions. One more source of the error is inhomogeneity of the dopant distribution over the crystal. These two factors reduce the possible accuracy of the JTE parameters evaluation and further comparison of different complexes in various matrices.

However, we have found the parameters which are not depend upon concentration. These parameters are relaxation time and the ratio of the linear vibronic coupling constants. The first one is determined from the shape of the attenuation or dispersion curves but not on the scale of their variation. The second parameter is concentration independent since both the coupling constants have linear dependence on concentration of the JT complexes and their ratio does not depend on it.

Finally, one can conclude that in the studied crystals: (i) the linear vibronic coupling constants characterizing the JT centers are approximately equal if to speak about their absolute values; (ii) activation energy characterizing the crystals is in the range of 90-400 cm^{-1} ; (iii) the order of the absolute value of the linear vibronic coupling constants F_E and F_T is 10^{-4} dyn.

Further prospects for the development of the topic

Further developments lie both in the field of fundamental and applied research. The unsolved fundamental problem is the study of the APES in other fluorite-type matrices with more heavy cations, namely, CdF_2 and BaF_2 doped with 3*d* metals. Finally, the crystal with high barriers and low relaxation rate will be found. Such crystal can have practical application as the element basis of quantum computers.

LIST OF REFRENCES

1. Jahn, H. A. Stability of polyatomic molecules in degenerate electronic states I—Orbital degeneracy / H. A. Jahn, E. Teller // Proc. R. Soc. London. Ser. A-Math. Phys. Sci. – 1937. – V. 161 – № 905. – P. 220–235.
2. Liu, H. Pseudo-Jahn-Teller Effect and Magnetoelastic Coupling in Spin-Orbit Mott Insulators / H. Liu, G. Khaliullin // Phys. Rev. Lett. – 2019. – V. 122 – № 5. – P. 057203.
3. Subramanian, S. Density functional theory studies of structural distortion in lone pair substituted $LuMnO_3$ / S. Subramanian, S. Anandan, B. Natesan // Mater. Today Commun. – 2020. – V. 24 – P. 101079.
4. Jin, C. Two-dimensional non-van der Waals magnetic layers: functional materials for potential device applications / C. Jin, L. Kou // J. Phys. D. Appl. Phys. – 2021. – V. 54 – № 41. – P. 413001.
5. Kim, Y.-J. Raman imaging of ferroelastically configurable Jahn–Teller domains in LaMnO3 / Y.-J. Kim, H.-S. Park, C.-H. Yang // npj Quantum Mater. – 2021. – V. 6 – № 1. – P. 62.
6. Chen, W.-T. Striping of orbital-order with charge-disorder in optimally doped manganites / W.-T. Chen, C.-W. Wang, C.-C. Cheng, Y.-C. Chuang, A. Simonov, N. C. Bristowe, M. S. Senn // Nat. Commun. – 2021. – V. 12 – № 1. – P. 6319.
7. Merten, S. Magnetic-Field-Induced Suppression of Jahn-Teller Phonon Bands in $(La_{0.6}Pr_{0.4})_{0.7}Ca_{0.3}MnO_3$: the Mechanism of Colossal Magnetoresistance shown by Raman Spectroscopy / S. Merten, O. Shapoval, B. Damaschke, K. Samwer, V. Moshnyaga // Sci. Rep. – 2019. – V. 9 – № 1. – P. 2387.
8. Polinger, V. Pseudo Jahn-Teller effect in permittivity of ferroelectric perovskites / V. Polinger, I. B. Bersuker // J. Phys. Conf. Ser. – 2017. – V. 833 – P. 012012.
9. Mihalik, M. Cooperative Jahn-Teller effect in $NdMn_{1-x}Fe_xO_{3+\delta}$ ($0 \leq x \leq 0.2$) / M. Mihalik, K. Csach, V. Kavečanský, M. Mihalik // J. Alloys Compd. –

2021. – V. 857 – P. 157612.

10. Mohanty, P. Role of Ni substitution on structural, magnetic and electronic properties of epitaxial $CoCr_2O_4$ spinel thin films / P. Mohanty, S. Chowdhury, R. J. Choudhary, A. Gome, V. R. Reddy, G. R. Umapathy, S. Ojha, E. Carleschi, B. P. Doyle, A. R. E. Prinsloo, C. J. Sheppard // Nanotechnology – 2020. – V. 31 – № 28. – P. 285708.
11. Hong, Y. Local-electrostatics-induced oxygen octahedral distortion in perovskite oxides and insight into the structure of Ruddlesden–Popper phases / Y. Hong, P. Byeon, J. Bak, Y. Heo, H-S. Kim, H. Bin Bae, S-Y. Chung // Nat. Commun. – 2021. – V. 12 – № 1. – P. 5527.
12. Viswanathan, M. Insights on the Jahn–Teller distortion, hydrogen bonding and local-environment correlations in a promised multiferroic hybrid perovskite / M. Viswanathan // J. Phys. Condens. Matter – 2019. – V. 31 – № 45. – P. 45LT01.
13. Bersuker, I. B. Perovskite Crystals: Unique Pseudo-Jahn–Teller Origin of Ferroelectricity, Multiferroicity, Permittivity, Flexoelectricity, and Polar Nanoregions / I. B. Bersuker, V. Polinger // Condens. Matter – 2020. – V. 5 – № 4. – P. 68.
14. Chandra, M. Enhancement of magnetoelectric coupling in Cr doped Mn2O3 / M. Chandra, S. Yadav, R. Rawat, K. Singh // J. Phys. Condens. Matter – 2020. – V. 32 – № 29. – P. 295703.
15. Thang, P. D. Electronic structure and multiferroic properties of (Y, Mn)-doped barium hexaferrite compounds / P. D. Thang, N. H. Tiep, T. A. Ho, N. D. Co, N. T. M. Hong, Q. V. Dong, B. W. Lee, T. L. Phan, N. T. Dang, D. T. Khan, D. S. Yang // J. Alloys Compd. – 2021. – V. 867 – P. 158794.
16. Angeli, M. Valley Jahn-Teller Effect in Twisted Bilayer Graphene / M. Angeli, E. Tosatti, M. Fabrizio // Phys. Rev. X – 2019. – V. 9 – № 4. – P. 041010.
17. Liu, D. Dynamical Jahn-Teller effect of fullerene anions / D. Liu, N. Iwahara, L. F. Chibotaru // Phys. Rev. B – 2018. – V. 97 – № 11. – P.

115412.

18. Oliete, P. B. A Jahn-Teller study of the orthorhombically distorted Cr^{2+} centre in SrF_2 and CaF_2 / P. B. Oliete, C. A. Bates, J. L. Dunn // J. Phys. Condens. Matter – 1999. – V. 11 – № 12. – P. 2579–2588.
19. Cartlidge, E. The light fantastic / E. Cartlidge // Science (80). – 2018. – V. 359 – № 6374. – P. 382–385.
20. Gong, Q. Theoretical study on near UV and visible optical absorption characteristics of Ti-doped α-Al_2O_3 single crystals / Q. Gong, C. Zhao, S. Li, G. Zhao, M. Xu, Y. Hang // Mater. Today Commun. – 2021. – V. 28 – P. 102506.
21. Gilardoni, C. M. Hyperfine-mediated transitions between electronic spin-1/2 levels of transition metal defects in SiC / C. M. Gilardoni, I. Ion, F. Hendriks, M. Trupke, C. H. van der Wal // New J. Phys. – 2021. – V. 23 – № 8. – P. 083010.
22. Stokes, G. G. XXX. On the change of refrangibility of light / G. G. Stokes // Philos. Trans. R. Soc. London – 1852. – V. 142 – P. 463–562.
23. Capper P. Bulk Crystal Growth of Electronic, Optical and Optoelectronic Materials / P. Capper. – Wiley, New York. – 2005.
24. Rost F. Photography with a Microscope / F. Rost, R. OldField. – Cambridge, Cambridge Univ. Press. – 2000.
25. Ray S. F. Scientific Photography and Applied Imaging / S. F. Ray. – Focal Press New York, London. – 1999.
26. Bersuker I. B. Electronic Structure and Properties of Transition Metal Compounds: Introduction to the Theory / I. B. Bersuker. – Wiley, New York. – 2010.
27. Ishikawa, H. Ligand dependent magnetism of the Jeff = 3/2 Mott insulator Cs_2MX_6 (M = Ta, Nb, X = Br, Cl) / H. Ishikawa, T. Yajima, A. Matsuo, K. Kindo // J. Phys. Condens. Matter – 2021. – V. 33 – № 12. – P. 125802.
28. Zaripov, M. M. Jahn-Teller chromium ions in SrF_2 crystals: EPR study in the range 9.3-300 GHz / M. M. Zaripov, V. F. Tarasov, V. A. Ulanov, G. S.

Shakurov, M. L. Popov // Phys. Solid State – 1995. – V. 37 – № 3. – P. 437–440.

29. Oliete, P. B. Structure of the Jahn-Teller distorted Cr^{2+} defect in SrF_2:Cr by electron-spin-echo envelope modulation / P. B. Oliete, V. M. Orera, P. J. Alonso // Phys. Rev. B – 1996. – V. 54 – № 17. – P. 12099–12108.
30. Hoffmann, S. K. Molecular structure and dynamics of off-center Cu^{2+} ions and strongly coupled Cu^{2+} – Cu^{2+} pairs in BaF_2 crystals: Electron paramagnetic resonance and electron spin relaxation studies / S. K. Hoffmann, J. Goslar, S. Lijewski, V. A. Ulanov // J. Chem. Phys. – 2007. – V. 127 – № 12. – P. 124705.
31. Zhang, H-M. Investigations on the EPR parameters and defect structures due to Jahn-Teller effect for the Cu^{2+} and Ni^{+} centers in $LiNbO_3$ / H-M. Zhang, W-B. Xiao // J. Alloys Compd. – 2018. – V. 745 – P. 586–591.
32. Luthi B. Physical Acoustics in the Solid State / B. Luthi. – Berlin, Springer. – 2005.
33. Sturge M. D. The Jahn-Teller Effect in Solids / F. Seitz, D. Turnbull, H. Ehrenreich // New York, London: Academic Press. – 1968. pp. 91–211 .
34. Gyorgy, E. M. Observation of Jahn-Teller Tunneling by Acoustic Loss / E. M. Gyorgy, M. D. Sturge, D. B. Fraser, R. C. LeCraw // Phys. Rev. Lett. – 1965. – V. 15 – № 1. – P. 19–22.
35. Sturge, M. D. Acoustic Behavior of the Jahn-Teller Ion Ni^{3+}in Al_2O_3 / M. D. Sturge, J. T. Krause, E. M. Gyorgy, R. C. LeCraw, F. R. Merritt // Phys. Rev. – 1967. – V. 155 – № 2. – P. 218–224.
36. Gudkov, V. V. Ultrasonic evaluation of the Jahn–Teller effect parameters. Application to ZnSe:Cr^{2+} / V. V Gudkov, I. B. Bersuker, I. V. Zhevstovskikh, Y. V. Korostelin, A. I. Landman // J. Phys. Condens. Matter – 2011. – V. 23 – № 11. – P. 115401.
37. Averkiev N. S. Fluorite structure, chemistry and application / N. S. Averkiev, I. B. Bersuker, V. V. Gudkov, I. V. Zhevstovskikh, M. N. Sarychev, S. Zherllitsyn, Sh. Yasin, G. S. Shakurov, V. A. Ulanov, V. T.

Surikov // The Jahn-Teller effect in elastic moduli of cubic crystals: general theory and application to strontium fluorite doped with chromium ions. Nova Sci. Publ. Inc., New York. – 2019. P. 111–159.

38. Bersuker I. B. The Jahn–Teller Effect / I. B. Bersuker. – Cambridge, Cambridge Univ. Press. – 2006.
39. Bersuker, I. V. Jahn-Teller effect for T terms / I. V. Bersuker, V. Z. polinger // Sov. Phys-JETP. – 1974. – V. 39 – № 6. – P. 1023–1029.
40. Renner, R. Zur Theorie der Wechselwirkung zwischen Elektronen- und Kernbewegung bei dreiatomigen, stabförmigen Molekülen / R. Renner // Zeitschrift für Phys. – 1934. – V. 92 – № 3–4. – P. 172–193.
41. Van Vleck, J. H. The Jahn-Teller Effect and Crystalline Stark Splitting for Clusters of the Form XY_6 / J. H. Van Vleck // J. Chem. Phys. – 1939. – V. 7 – № 1. – P. 72–84.
42. Opik, U. Studies of the Jahn-Teller effect. I. A survey of the static problem / U. Opik and M. H. L. Pryce // Proc. R. Soc. London. Ser. A. Math. Phys. Sci. – 1957. – V. 238 – № 1215. – P. 425–447.
43. Liehr, A. D. Inherent configurational instability of octahedral inorganic complexes in Eg electronic states / A. D. Liehr, C. J. Ballhausen // Ann. Phys. (N. Y). – 1958. – V. 3 – № 3. – P. 304–319.
44. William L. Paramagnetic Resonance in Solids / L. William, S. Frederick, T. David. – New York, Acad. Press. – 1960.
45. Abragam, A. Theoretical Interpretation of Copper Fluosilicate Spectrum / A. Abragam, M. H. L. Pryce // Proc. Phys. Soc. Sect. A – 1950. – V. 63 – № 4. – P. 409–411.
46. Bleaney, B. Paramagnetic Resonance in Copper Fluosilicate / B. Bleaney, D. J. E. Ingram // Proc. Phys. Soc. Sect. A – 1950. – V. 63 – № 4. – P. 408–409.
47. Bleaney, B. The Cupric Ion in a Trigonal Crystalline Electric Field / B. Bleaney, K. D. Bowers // Proc. Phys. Soc. Sect. A – 1952. – V. 65 – № 8. – P. 667–668.
48. Longuet-Higgins, H. Studies of the Jahn-Teller effect .II. The dynamical

problem / H. C. Longuet-Higgins, U. Opik, M. H. L. Pryce, R. A. Sack // Proc. R. Soc. London. Ser. A. Math. Phys. Sci. – 1958. – V. 244 – № 1236. – P. 1–16.

49. Englman R. The Jahn–Teller Effect in Molecules and Crystals / R. Englman. – London, Wiley. – 1972.
50. Bersuker I. B. The Jahn-Teller effect, a bibliographic review / I. B. Bersuker. – New York, IFI/Plenum. – 1984.
51. Ham, F. S. Effect of Linear Jahn-Teller Coupling on Paramagnetic Resonance in a ^{2}E State / F. S. Ham // Phys. Rev. – 1968. – V. 166 – № 2. – P. 307–321.
52. Tucker J. W. Microwave ultrasonics in solid state pjysics / J. W. Tucker, V. W. Rampton. – North-holl. Publ. Co., Amsterdam. – 1972.
53. Sturge, M. D. Jahn-Teller Effect in the $^4T_{2g}$ Excited State of V^{2+} in MgO / M. D. Sturge // Phys. Rev. – 1965. – V. 140 – № 3A. – P. A880–A891.
54. Mac, W. Magnetic properties of Cr-based diluted magnetic semiconductors / W. Mac, A. Twardowski, P. J. T. Eggenkamp, H. J. M. Swagten, Y. Shapira, M. Demianiuk // Phys. Rev. B – 1994. – V. 50 – № 19. – P. 14144–14154.
55. Boonman, M. E. J. High-magnetic-field EPR of Cr-based diluted magnetic semiconductors / M. E. J. Boonman, W. Mac, A. Twardowski, A. Wittlin, P. J. M. van Bentum, J. C. Maan, M. Demianiuk // Phys. Rev. B – 2000. – V. 61 – № 8. – P. 5358–5368.
56. Landau L. D. Theory of Elasticity / L. D. Landau, E. M. Lifshitz. – Amsterdam, Elsevier. – 2007.
57. Landau L. D. Statistical Physics / L. D. Landau, E. M. Lifshitz. – Amsterdam, Elsevier. – 2013.
58. Zener C. Elasticity and Anelasticity of Metals / C. Zener. – Univ. Chicago, Chicago Press. – 1948.
59. Pomerantz, M. Ultrasonic loss and gain mechanisms in semiconductors / M. Pomerantz // Proc. IEEE – 1965. – V. 53 – № 10. – P. 1438–1451.
60. Gudkov V. V. Ultrasonic consequences of the Jahn–Teller Effect. In The

Jahn–Teller Effect Fundamentals and Implications for for physics and chemistry edited by H. Koppel, D. R. Yarkony, H. Barentzen, pp. 743. Springer, New York, 2009.

61. Mcskimin H. J. Ultrasonic Methods for Measuring the Mechanical Properties of Liquids and Solids. In physical acoustic Principles and Methods edited by W. P. MASON, Acad. Press. New York London, 1964.
62. Gudkov V.V. Magnetoacoustic Polarization Phenomena in Solids / V.V. Gudkov, J. D. Gavenda. – Springer-Verlag, New York. – 2000.
63. Gudkov, V. Low temperature ultrasonic investigation of ZnSe crystals doped with Ni / V. Gudkov, A. Lonchakov, V. Sokolov, I. Zhevstovskikh, N. Gruzdev // Phys. status solidi – 2005. – V. 242 – № 3. – P. R30–R32.
64. Gudkov, V. V. Relaxation in ZnSe:Cr^{2+} investigated with longitudinal ultrasonic waves / V. V. Gudkov, A. T. Lonchakov, V. I. Sokolov, I. V. Zhevstovskikh // Phys. Rev. B – 2006. – V. 73 – № 3. – P. 035213.
65. Gudkov, V. V. Ultrasonic evaluation of the Jahn–Teller effect parameters. Application to ZnSe:Cr^{2+} / V. V Gudkov, I. B. Bersuker, I. V. Zhevstovskikh, Y. V. Korostelin, A. I. Landman // J. Phys. Condens. Matter – 2011. – V. 23 – № 11. – P. 115401.
66. Gudkov, V. V. Ultrasonic investigation of ZnSe:V^{2+} and ZnSe:Mn^{2+}: Lattice softening and low-temperature relaxation in crystals with orbitally degenerate states / V. V. Gudkov, A. T. Lonchakov, V. I. Sokolov, I. V. Zhevstovskikh, V. T. Surikov // Phys. Rev. B – 2008. – V. 77 – № 15. – P. 155210.
67. Gudkov, V. Ultrasonic investigation of the Jahn-Teller effect in ZnSe and ZnTe crystals doped with 3d lons / V. Gudkov, A. Lonchakov, V. Sokolov, I. Zhevstovskikh // Korean Phys. Soc. – 2008. – V. 53 – № 1. – P. 63–66.
68. Gudkov, V. V. Ultrasonic investigations of the Jahn–Teller effect in a ZnSe:Fe^{2+} crystal / V. V. Gudkov, A. T. Lonchakov, I. V. Zhevstovskikh, V. I. Sokolov, V. T. Surikov // Low Temp. Phys. – 2009. – V. 35 – № 1. – P. 76–78.
69. Sarychev, M. N. Magnetoelasticity of a Jahn–Teller Subsystem in

Chromium-Doped II–VI Crystals / M. N. Sarychev, I. V. Zhevstovskikh, Yu. V. Korostelin, V. T. Surikov, N. S. Averkiev, V. V. Gudkov // J. Exp. Theor. Phys. – 2023. – V. 136 – № 1. – P. 80–88.

70. Zaripov, M. M. Jahn-teller chromium ions in CdF_2 and CaF_2 crystals: An EPR spectroscopic study in the frequency range 9.3–300 GHz / M. M. Zaripov, V. F. Tarasov, V. A. Ulanov, G. S. Shakurov // Phys. Solid State – 2002. – V. 44 – № 11. – P. 2050–2054.
71. Alcalá, R. Cr^+ and Cr^{3+} defects in CaF_2 and SrF_2 / R. Alcalá, P. J. Alonso, V. M. Orera, H. W. den Hartog // Phys. Rev. B – 1985. – V. 32 – № 6. – P. 4158–4163.
72. Seijo, L. Ab initio model potential study of local distortions around Cr^+ and Cr^{3+} defects in fluorite / L. Seijo, Z. Barandiarán // J. Chem. Phys. – 1991. – V. 94 – № 12. – P. 8158–8164.
73. Asadullina, N. Y. EPR of trivalent chromium centers with monoclinic symmetry in SrF_2 crystals / N. Y. Asadullina, M. M. Zaripov, V. A. Ulanov // Phys. Solid State – 1997. – V. 39 – № 2. – P. 265–267.
74. Ulanov, V. A. Trimers of bivalent copper impurity ions in CaF_2 crystals: The structure and mechanism of formation / A. V. Ulanov, M. M. Zaripov, E. P. Zheglov, R. M. Eremina // Fiz. Tverd. Tela – 2003. – V. 45 – P. 73–77.
75. Hoffmann, S. K. Off-centre dynamic Jahn-Teller effect studied by electron spin relaxation of Cu^{2+} ions in SrF_2 crystal / S. K. Hoffmann, V. A. Ulanov // J. Phys. Condens. Matter – 2000. – V. 12 – № 8. – P. 1855–1866.
76. García Fernández, P. Cu^{2+} impurities in fluorite-type crystals: Mechanisms favoring an off-center motion / P. García Fernández, J. A. Aramburu, M. T. Barriuso, M. Moreno // Phys. Rev. B – 2004. – V. 69 – № 17. – P. 174110.
77. Kaiser, W. Infrared Properties of CaF_2, SrF_2, and BaF_2 / W. Kaiser, W. G. Spitzer, R. H. Kaiser, L. E. Howarth // Phys. Rev. – 1962. – V. 127 – № 6. – P. 1950–1954.
78. Bersuker, I. B. Jahn-Teller effect for T terms / I. B. Bersuker and V. Z. Polinger // Zh. Eksp. Teor. Fiz. – 1974. – V. 66 – P. 2078–2091.

79. Gehlhoff, W. Transition Metal Ions in Crystals with the Fluorite Structure / W. Gehlhoff, W. Ulrici // Phys. status solidi – 1980. – V. 102 – № 1. – P. 11–59.

80. Asadullina, N. Y. EPR of trivalent chromium centers with monoclinic symmetry in SrF_2 crystals / N. Y. Asadullina, M. M. Zaripov, V. A. Ulanov // Phys. solid state – 1997. – V. 39 – № 2. – P. 265–267.

81. Aramburu, J. A. Big off-center displacements of ions in insulators: The JahnTeller ion Ni^+ in CaF_2 / J. A. Aramburu, P. García Fernández, M. T. Barriuso, M. Moreno // Phys. Rev. B – 2003. – V. 67 – № 2. – P. 020101.

82. Aramburu, J. A. Off-centre motion in doped cubic oxides: A general view on the instability / J. A. Aramburu, P. Garcia-Fernandez, M. Moreno // Chem. Phys. – 2015. – V. 460 – P. 83–89.

83. Huffman, D. R. Specific Heat and Elastic Constants of Calcium Fluoride at Low Temperatures / D. R. Huffman, M. H. Norwood // Phys. Rev. – 1960. – V. 117 – № 3. – P. 709–711.

LIST OF MAIN PUBLICATIONS ON THE DISSERTATION TOPIC

Articles in peer-reviewed scientific journals, determined by the Higher Attestation Commission and the Attestation Council of UrFU

A1. Sarychev, M. N. Adiabatic potential energy surface of the Jahn-Teller complexes in CaF_2:Ni^{2+} crystal determined from experiment on ultrasonic attenuation / M. N. Sarychev, **W. A. L. Hosseny**, A. S. Bondarevskaya, I. V. Zhevstovskikh, A. V. Egranov, O. S. Grunskiy, V. T. Surikov, N. S. Averkiev, V. V. Gudkov // J. Alloys Compd. – 2020. – V. 848. – P. 156167; 0.43 п.л/0,04 п.л. (scopus and web of science, **Q1**)

A2. Sarychev, M. N. Manifestation of the Jahn–Teller effect subject to quadratic $T\otimes(e+t_2)$ problem in ultrasonic attenuation. Case study of CaF_2 :Cr crystal with isovalent and aliovalent substitution / M. N. Sarychev, **W. A. L.**

Hosseny, I. V Zhevstovskikh, V. A. Ulanov, G. S. Shakurov, A. V Egranov, V. T. Surikov, N. S. Averkiev, V. V Gudkov // J. Phys.: Condens. Matter – 2022. – V. 34. – № 22. – P. 225401; 0.75 п.л/0,08 п.л. (scopus and web of science, **Q2**)

A3. Сарычев, М. Н. Аиабатический потенциал ян-теллеровских комплексов $Cu^{2+}F^{-}_{8}$ в кристалле флюорита / М. Н. Сарычев, **У. А. Л. Хоссени**, И. В. Жевстовских, В. А. Уланов, А. В. Егранов, В. Т. Суриков, Н. С. Аверкиев, В. В. Гудков // ЖЭТФ. – 2022. – 162. – С. 509–521; 0.81 п.л/0,1 п.л.

Sarychev, M. N. Adiabatic potential energy surface of Jahn–Teller Cu^{2+} complexes in a fluorite crystal / M. N. Sarychev, **W. A. L. Hosseny**, I. V. Zhevstovskikh, V. A. Ulanov, A. V. Egranov, V. T. Surikov, N. S. Averkiev, V. V. Gudkov // J. Exp. Theor. Phys. – 2022. – V. 135. – №4. – P. 473–483; 0.68 п.л/0,08 п.л. (scopus and web of science, **Q3**)

A4. Sarychev, M. N. Adiabatic potential energy surface of the Jahn-Teller complexes in SrF_2:Cr^{2+} crystal / M. N. Sarychev, **W. A. L. Hosseny**, A. S. Bondarevskaya, G. S. Shakurov, V. A. Ulanov, V. T. Surikov, I. V. Zhevstovskikh, N. S. Averkiev, V. V. Gudkov // AIP Conference Proceedings. – 2020. – V. 2313. – P. 030071; 0.5 п.л/0,05 п.л. (scopus)

A5. Sarychev, M. N. Contribution of the distorted Jahn-Teller complexes to the elastic moduli in fluorite crystal / M. N. Sarychev, **W. A. L. Hosseny**, V. A. Ulanov, A. V. Egranov, V. T. Surikov, I. V. Zhevstovskikh, N. S. Averkiev, V. V. Gudkov // AIP Conference Proceedings. – 2022. – V. 2466. – P. 030013; 0.43 п.л/0,05 п.л. (scopus)

List of reports at conferences

C1. Averkiev N.S, Bersuker I.B, Gudkov V.V, Sarychev M.N, Zhevstovskikh I.V, Bondarevskaya A.S, **Hosseny W.A.L**, Shutov I.S, Egranov A.V. Relaxation of ultrasound by impurity centers with the Jahn-Teller effect in

cubic crystals / XIV Russian Conference in semiconductor physics (RCS). Novisiberisc. – 2019. – P. 341; 0,15 / 0,09 п.л.

C2. **Hosseny W.A.L,** Sarychev M.N, Zhevstovskikh I.V, Shakurov G.S, Ulanov V.A., Averkiev N.S., Gudkov V.V. Jahn-Teller effect in strontium fluorite doped with chromium ions studied in ultrasonic experiment / XXIII Ural International Winter school of semiconductor physics (UIWSPS). Yekaterinburg. – 2020. – P. 341; 0,15 / 0,09 п.л.

C3. **Hosseny W.A.L**, Sarychev M.N, Zhevstovskikh I.V, Gudkov V.V. adiabatic Jahan-Teller potential complexes in a CaF2:Cr crystal / scientific session NRNU MEFI on the direction innovative nuclear technologies (NRNU MEFI). Snezhinsk. – 2020. – P. 174; 0,15 / 0,09 п.л.

C4. Sarychev M.N, **Hosseny W.A.L**., Ulanov V. A, Egranov A. V, Zhevstovskikh I.V, Averkiev N.S, Gudkov V.V. activation energy of the Jahn-Teller complexes in CaF_2:Cu^{2+} crystal / VII International Youth Scientific Conference Physics. Technology. Innovations. Yekaterinburg. – 2022. – P. 189; 0,15 / 0,09 п.л.

C5. Sarychev M.N, **Hosseny W.A.L**, Ulanov V. A, Shakurov G.S, Egranov A. V, Surikov V.T, Zhevstovskikh I.V, Averkiev N.S, Gudkov V.V. stabilization energies of the Jahn-Teller complexes in CaF_2:Cr^2 crystal / VII International Youth Scientific Conference Physics. Technology. Innovations. Yekaterinburg. – 2021. – P. 223; 0,15 / 0,09 п.л.

C6. **Hosseny W.A.L**, Sarychev M.N, Bondarevskaya A.S, Shakurov G.S, Ulanov V.A, Surikov V.T, Zhevstovskikh I.V, Averkiev N.S, Gudkov V.V, adiabatic potential energy surface of the Jahn-Teller complexes in SrF_2:Cr^{2+} crystal / VII International Youth Scientific Conference Physics. Technology. Innovations. Yekaterinburg. – 2020. – P. 191; 0,15 / 0,09 п.л.